Chapter 3: Molecular Ferroelectric Materials

Generating polar space group in Anilinium nitrate salt by its derivatization

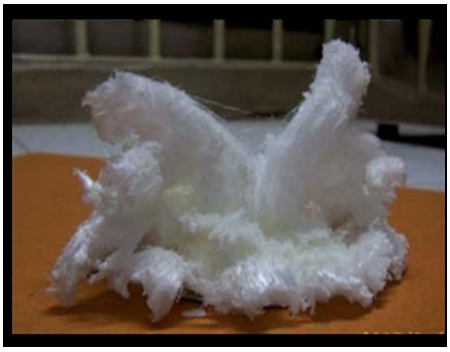

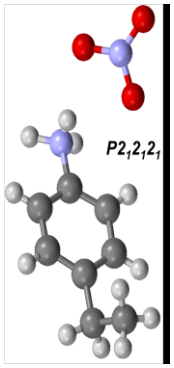

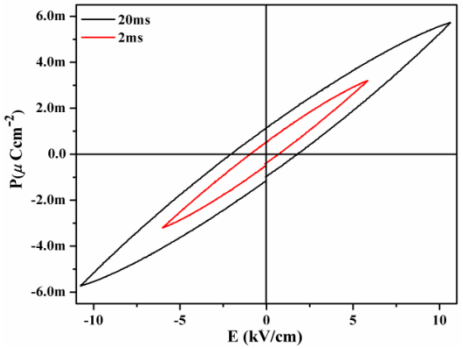

Materials found in non-centrosymmetric (NCS) or acentric crystal classes i.e. crystal classes lacking a center of inversion exhibit a variety of technologically important physical properties [1] such as piezoelectricity, ferroelectricity and pyroelectricity. In ferroelectric material, electric dipoles inherent in the atomic structure (between cation and anion) can couple with each other so that they align in parallel fashion, creating domains of aligned dipoles. These dipoles and consequently the domains can be reoriented and aligned with an applied electric field [2]. Spontaneous polarization observed in ferroelectric materials is reversed by an applied electric field which makes them useful in ferroelectric random access memory (FeRAM), nonlinear optical devices, piezoelectric devices and capacitors [3]. Such behaviour is observed in materials [4] such as $BaTiO_3$ (ionic structure, displasive), purely organic (charge transfer, order-disorder and/or displasive) and organic polymers (entanglement of polymers) after its discovery in K-tartrate.

Ferroelectricity is a phenomenon which was discovered in 1921 by J. Valasek [5] who investigated the dielectric properties of Rochelle salt ($NaKC_4H_4O_6.4H_2O$). Ferroelectricity has also been called Seignette electricity, as Seignette or Rochelle Salt (RS) as it was first separated by Elie Seignette (1655) in France, though pyroelectricity has been known since ancient times [6]. With respect to polarity ferroelectricity and pyroelectricity are same. Only, former shows reversible dipole moment (switchable) in the presence of an applied voltage. Thus all ferroelectric materials are pyroelectric, but the converse is not true. Another feature that is observed in some, but not all ferroelectric materials is dielectric anomaly at the Curie temperature. A maximum in the dielectric constant is often observed at the Curie temperature. This temperature indicates a phase-change to a centrosymmetric non-polar, i.e. non-ferroelectric, structure.

The key factor for obtaining ferroelectricity is the change of structure or framework into polar and/or chiral space group by variation of physical parameters. Ferroelectric materials must possess a permanent dipole moment and capable of having this moment reversed in the presence of an applied voltage. This occurs only if the material crystallizes in one of ten polar crystal classes (1, 2, 3, 4, 6, m, mm2, 3m, 4mm, or 6mm). A scheme depicting the acentric crystal class in bold letters appears in Scheme-3.1.

- $T\ T_h\ O\ T_d\ O_h$
- $\boldsymbol{C_4}\ S_4\ C_{4h}\ D_4\ \boldsymbol{C_{4v}}\ D_{2d}\ D_{4h}$
- $D_2\ \boldsymbol{C_{2v}}\ D_{2h}$
- $\boldsymbol{C_2}\ \boldsymbol{C_s}\ C_{2h}$
- $\boldsymbol{C_1}\ C_i$
- $\boldsymbol{C_3}\ S_6\ D_3\ \boldsymbol{C_{3v}}\ D_{3d}$
- $\boldsymbol{C_6}\ C_{3h}\ C_{6h}\ D_6\ \boldsymbol{C_{6v}}\ D_{3h}\ D_{6h}$

Scheme 3.1: 10 polar point groups

The crystal classification of a material has immediate implications for ferroelectric effects. There are total 32 crystal classes. 11 of them possess centre of symmetry (centrosymmetric and chiral, and therefore possess a 'handedness') and cannot support ferroelectricity while remaining 21, the *O*-point group (432) also excludes ferroelectricity. The remaining 20 classes all exhibit the *piezoelectric effect.* Only 10 are *polar*, i.e. they contain a dipole moment and five crystal classes- 1, 2, 3, 4, and 6 exhibit chiral and polar symmetry.

Chiral compounds are the obvious short way to acentric crystals. However, also in this case the probability of getting a polar crystal is low, as witnessed by the fact that the most frequent acentric space group is $P2_12_12_1$ (class 222) which is nonpolar. Moreover, even within the set of compounds which do crystallize in a polar space group (e.g. $P2_1$, $Pca2_1$, and $Pna2_1$), in many cases the independent molecule is placed with its charge transfer axis perpendicular to the polar binary screw axis [7], giving rise to vanishing bulk nonlinearities.

In a polar crystal there is a direction called the polar axis of the crystal which is not transformed in the opposite direction by any symmetry operation of the crystal class [8]. Only 10–15% achiral organic compounds crystallizes in non-centrosymmetric space groups [9]. This finding is consistent with the classic analysis of Kitaigorodsky, who showed that many space groups allowing the close packing of molecules are centrosymmetric [10]. Additionally, in crystals of dipolar organic molecules in which dipole–dipole intermolecular forces play a relevant role, the arrangement with strictly anti-parallel adjacent dipoles, obtained by the inversion center, is energetically favored.

The signature of this reversible change in the structure due to displasive (I) and/or order-disorder (II) transition is easily observed in thermal studies. In type I (Figure 3.1 (I)), relative displacement of the ions creates spontaneous polarization e.g. inorganic oxides ($BaTiO_3$). In type II (Figure 3.1 (II)), reorientation of ions/ molecules generates polarisation and hence ferroelectricity. $NaNO_2$ is a typical ferroelectric of type II, in which reorientation of the dipolar NO_2^- ions generates ferroelectricity. Most of the ferroelectric crystals often show both displacive and order-disorder characteristics. According to the Aizu rule, only 88 ferroelectric phase transitions, i.e. transitions from a paraelectric phase to a ferroelectric one should be possible (Table 3.1). In Aizu notation, for e.g. 2/*mFm*, the *F* means ferroelectric phase transition, and the point group is 2/*m* in the paraelectric phase and *m* in the ferroelectric phase.

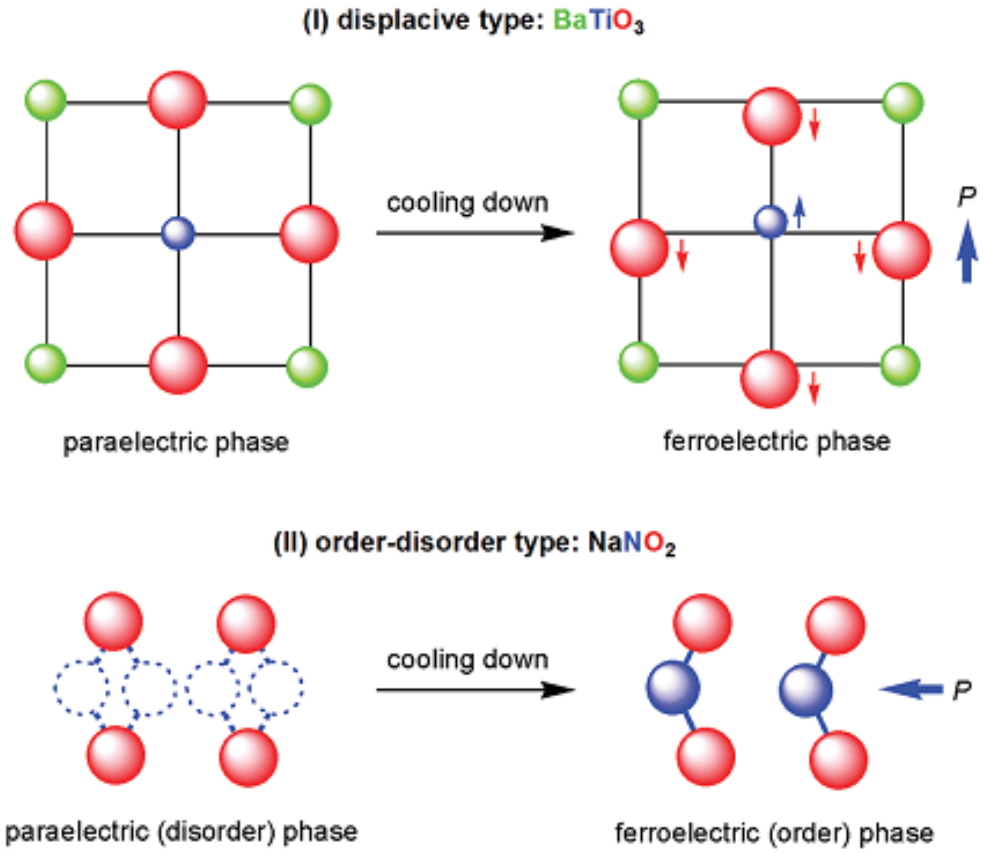

Fig. 3.1: Schematic illustrations for the displacive-type (I) and order disorder (II)-type ferroelectrics

Table 3.1: 88 possible ferroelectric phase transitions with Aizu notation

Triclinic	$\bar{1}F1$ (1)
Monoclinic	$2F1$ (2/2); $mF1$ (2/2); $2/mF1$ (2); $2/mFm$(1); $2/mF2$ (1)
Orthorhombic	$222F1$ (4/2); $222F2$ (1); $mm2F1$ (4/2); $mm2Fm$(2/2); $mmmF1$ (4); $mmmFm$(2); $mmmFmm2$ (1)
Trigonal	$3F1$ (3/2); $\bar{3}F1$ (3); $\bar{3}F3$ (1); $32F1$ (6/2); $32F2$ (3/2); $32F3$ (1); $3mF1$ (6/2); $3mFm$(3/2); $\bar{3}mF1$ (6); $\bar{3}mF2$ (3); $\bar{3}mFm$(3); $\bar{3}mF3m$ (1)
Tetragonal	$4F1$ (4/2); $\bar{4}F1$ (4/2); $\bar{4}F2$ (1); $4/mF1$ (4); $4/mFm$(2); $4/mF4$ (1); $422F1$ (8/2); $422F2$ (2); $422F4$ (1); $4mmF1$ (8/2); $4mmFm$(4/2); $\bar{4}2mF1$ (8/2); $\bar{4}2mF2$ (2); $\bar{4}2mFm$(4/2); $\bar{4}2mFmm2$ (1); $4/mmmF1$ (8); $4/mmmFm$(s) (4); $4/mmmFm$(p) (4); $4/mmmFmm2$ (2); $4/mmmF4mm$ (1)
Hexagonal	$6F1$ (6/2); $\bar{6}F1$ (6/2); $\bar{6}Fm$(3/2); $\bar{6}F3$ (1); $6/mF1$ (6); $6/mFm$(3); $6/mF6$ (1); $622F1$ (12/2); $622F2$ (3); $622F6$ (1); $6mmF1$ (12/2); $6mmFm$(6/2); $\bar{6}m2F1$ (12/2); $\bar{6}m2Fm$(s) (6/2); $\bar{6}m2Fm$(p) (6/2); $\bar{6}m2Fmm2$ (3/2); $\bar{6}m2F3m$ (1); $6/mmmF1$ (12); $6/mmmFm$(s) (6); $6/mmmFm$(p) (6); $6mmmFmm2$ (3); $6/mmmF6mm$ ($\bar{1}$)
Cubic	$23F1$ (12/2); $23F2$ (3); $23F3$ (4/2); $m3F1$ (12); $m3Fm$(6); $m3Fmm2$ (3); $m3F3$ (4); $432F1$(24/2); $432F2$ (6); $432F4$ (3); $432F3$ (4); $\bar{4}3mF1$ (24/2); $\bar{4}3mFm$(12/2); $\bar{4}3mFmm2$ (3); $\bar{4}3mF3m$ (4/2); $m3mF1$ (24); $m3mFm$(s) (12); $m3mFm$(p) (12) $m3mFmm2$ (6); $m3mF4mm$ (3); $m3mF3m$ (4)

***The s and p represent the polar and nonpolar symmetric axes, respectively. The number in the round bracket denotes the number of equivalent unique ferroelectric directions.**

However, in the true ferroelectricity, a spontaneous polarization (*P*s) is arising from the collective alignment of intrinsic dipole moments in a compound. A structural transition from high temperature-high symmetry paraelectric phase to low temperature-low symmetry ferroelectric phase have been occurred due to the presence of polar state in a compound. During this process, some of the high temperature phase symmetry elements are disappeared below *T*c (transition temperature) upon cooling, thus it becomes essential to introduce an order parameter (*P*s -ferroelectric system) as a measure of the degree of order in the system. For a ferroelectric system undergoing phase transition, a first-order phase transition is observed due to the discontinuous change of the *P*s, to the other hand a second-order (continuous) phase transition is observed due to continuous change of the *P*s. According to Landau theory, halving of the symmetric elements typically leads to a second-order phase transition. The Curie symmetry principle tells us that the space group of the ferroelectric phase must be a subgroup of the paraelectric phase. There are 18 uniaxial ferroelectric phase transitions as depicted in scheme 3.2.

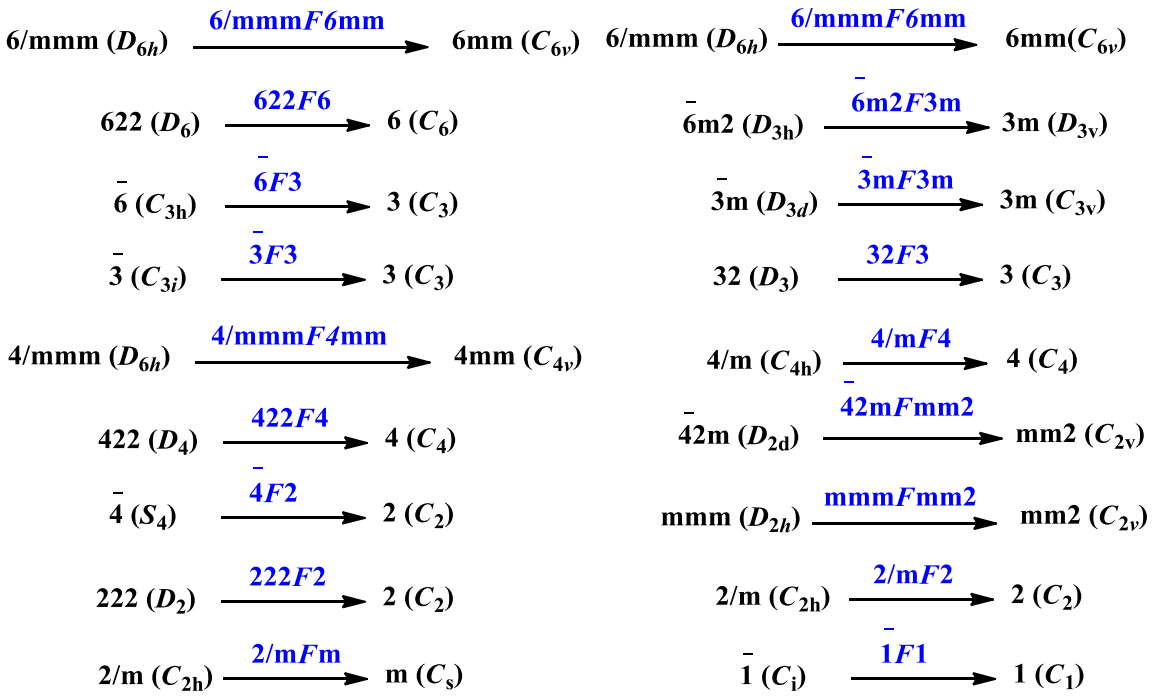

Scheme 3.2: 18 uniaxial ferroelectric phase transitions with Aizu notations.

The former transition (displasive (I)) is explored quite well for designing novel materials in last two decades, where ionic displacement played an important role. To our surprise, the latter (order-disorder (II)) requirement is not used or studied by synthetic chemists as a challenge, a *prima fascia* of 'molecular materials'. The reversibility and transition into non-centrosymmetric space group of these interactions with minimal energy requirement is the 'key' to design. Here, we will show our results where we introduced 'molecular' or 'organic' character to achieve ferroelectricity in traditional KNO_3 type ferroelectrics.

Motivation: In **KNO_3**, K^+ acts as stator and rotations of NO_3^- are responsible for ferro-electricity in its reentrant high temperature phase only. To observe this transition at room temperature we employed molecular strategy (a) by using molecular stator, that is organic cation, and (b) modulating overall crystallization in chiral space group.

Generating polar space group in Anilinium nitrate salt by its derivatization

Abstract:

This chapter deals with designing, crystallization and synthesis of five new anilinium nitrate compounds from aniline and its derivatives as shown below, of general formula R-NH_3NO_3, [where, R-NH_3 = Aniline (**1a/1b**), 4-methyl aniline (**2a/2b**), 4-ethyl aniline (**3a/2b**), 4-propyl aniline (**4b**)and 4-isopropyl aniline (**5b**). Compounds 1a, 2a, and 3a were crystallized from gel-mediated process, while 1b, 2b, 3b, 4b, and 5b by slow evaporation method. All compounds were investigated for thermal analyses, electric property and single crystal XRD. DSC measurement showed reversible solid-solid phase transitions at high temperature (HT) in all compounds except in **4b**. PE-Loop study suggested only gel hair crystals (1a and 3a) with ferroelectric phase at room temperature (RT).

Compound **1a** and **1b** crystallized in non chiral (non polar) orthorhombic space group *Pbca* with cell dimensions a = 10.1448(8) Å, b = 9.2781(15) Å, c = 16.147(2) Å, α= β= γ = 90º, V = 1519.9(3) $Å^3$ and Z = 8 for **1a** while a = 10.158 (2) Å, b = 9.277 (2) Å, c = 16.177 (3) Å, α= β= γ = 90º, V = 1524.5 (5) $Å^3$ and Z = 8 for **1b**.

Compound **2b** crystallized in non chiral monoclinic space group *P*21/n with cell dimensions a = 5.667 (5) Å, b = 8.576 (8) Å, c = 17.619 (14) Å, β=99. 026 (5)º, V = 845.87 (13) $Å^3$ and Z = 4.

Compound **3a** crystallised in chiral space group $P2_12_12_1$ (orthorhombic) with unit cell dimensions a= 5.559(2) Å, b = 9.010(6) Å, c = 19.472(9) Å, α= β= γ = 90º, V= 975.3(9) $Å^3$ and Z = 4.

Compound **3b-M** and **3b-P** are crystallized in orthorhombic space group $P2_12_12_1$, chiral (polar) space group, with unit cell dimensions for **3M**, a= 5.54536 (14) Å, b = 19.4934 (5) Å, c = 9.0081 (2) Å, α= β= γ = 90º, V= 973.76 (4) $Å^3$ and Z = 4; for **3P**, a=5. 597 (3) Å, b= 9.129 (5) Å, c = 19.608 (10) Å, α= β= γ = 90º, V= 1002.0 (9) $Å^3$ and Z = 4.

Variable temperature crystal structure of **3b** showed the transition from $P2_12_12_1$ to *Pbca* space group with unit cell dimensions a = 9.4724(15) Å, b = 10.5203(14) Å, c = 20.297(2) Å, α= β= γ = 90º, V = 2022.65 Å^3 and Z = 8.

Compound **4b** crystallized in non chiral orthorhombic space group *Pbca* with cell dimensions a = 9.7381 (2) Å, b = 10.9519 (3) Å, c = 19.608 (10) Å, α= β= γ = 90º, V = 2145.93 (10) Å^3 and Z = 8 while compound **5b** crystallized in non chiral monoclinic space group *P*21/c with cell dimensions a = 5.46121 (19) Å, b = 19.5309 (7) Å, c = 10.0581 (4) Å, β= 103.031 (3)º, V = 1045.19 (7) Å^3 and Z = 4.

Single crystal XRD studies revealed presence of TWO helical chains with opposite hydrogen bonding in all the compounds. Compound **2b** and **5b** have opposite hydrogen bonding helical chains due to which polarity cancels out and it crystallized in the non polar space group. Interestingly, these helical chains get separated, spontaneous resolution, with formation of conglomerate crystals for **3a**/**3b**. The high temperature crystal structure of compound **3b** confirms phase transition and molecular rearrangement results into formation of non polar space group i.e. centrosymmetric space group *Pbca.*

3.1 Introduction

Potassium nitrate exists in three different polymorphic forms [11]. Form II is stable at 299K contain α-phase, aragonite type structure and crystallized into orthorhombic *Pmcn* with a = 5.414 Å, b = 9.164 Å and c = 6.431Å. Ferroelectricity is observed in phase-III (γ-KNO_3, rhombohedral, space group *R3m* with a = 5.43Å and c = 9.112Å), a reentrant phase, in KNO_3 when it is heated above 483K to phase I (C_3 or D_6 symmetric) from stable phase II (β-KNO_3, rhombohedral, space group *Pnma,* calcite type with a = 5.42Å and c = 19.41Å*)* at RT. The driving force observed for the ferroelectricity is the order-disorder phenomena due to asymmetric NO_3^- vibrations [12]. Expansion of phase-III, ferroelectric character, was carried out by making thin films [13], nanoparticles and by dispersion in solid matrix [14].

Our strategy is based on substituting cation K^+, by organic cation, anilinium group. Thus, we synthesized and studied anilinium nitrate, which showed structural similarity to KNO_3, alternately stacked and equidistant cation and NO_3^- in a chain/column with no resultant polarization. One can induce ferroelectricity by making the structure non-centrosymmetric. In this work, we will explain our 'molecular' efforts to induct ferroelectricity by (a) altering electron accepting power on cation aromatic ring, a typical synthetic strategy; (b) growing polymorphs. To our best knowledge, this is a first time synthetic as well as polymorphic aspects are used to 'modulate' and 'observe' ferroelectricity. This will open up field for synthetic chemist to explore real 'molecular materials.

Crystal growth in gels is received wide attention in the recent past [15]. Various modifications of the gel method have been used to grow many crystals with a high degree of perfection [16]. The gel growth technique appeared quite attractive for growing crystals on account of its unique advantages in terms of crystals produced and the simplicity of the process. In our previous work, we reported hair like crystal growth of anilinium nitrate from gel. Powder X-ray diffraction of hair like crystals and sugar like crystals of anilinium nitrate are different. Hence we studied there structural and electrical properties as a polymorphs/habits.

The main goal of this chapter is to growing crystals under different conditions to obtain

polymorphs. 'Molecular' nature can be observed by tuning non-covalent interaction driven design synthetic strategy or by following different crystallisation procedure to form polymorphs. Hence we show application of both these aspects for observing 'ferro-electric' and 'ferroelastic' behaviour.

3.2 Experimental

3.2.1 Materials and Methods:

All reagents were commercially purchased. Aniline and 4-methyl aniline were from spectrochem and 4-ethyl aniline, 4-propyl aniline and 4-isopropyl aniline were from Across chemicals and used without further purification. Aniline was distilled at its boiling point and used. Doubly deionized water was used for the synthesis.

3.2.2 Syntheses of compounds:

Scheme: 3.3

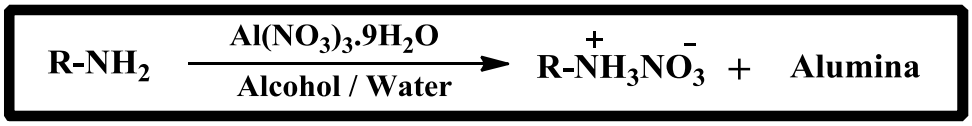

Where,

$R\text{-}NH_2$ =

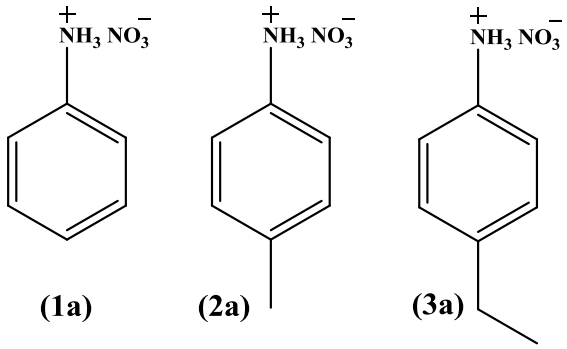

(1a) (2a) (3a)

Freshly distilled aniline was added directly into the methanolic solution of $Al(NO_3)_3.9H_2O$ in the 3 : 1 molar ratio. This mixture yielded a translucent gel. The gel was filtered and kept aside. After 1 h, white hair-like crystals were developed from filtered gel, growing up to 10–13 cm long in about 8–10 h, as shown in Figure 3.2.

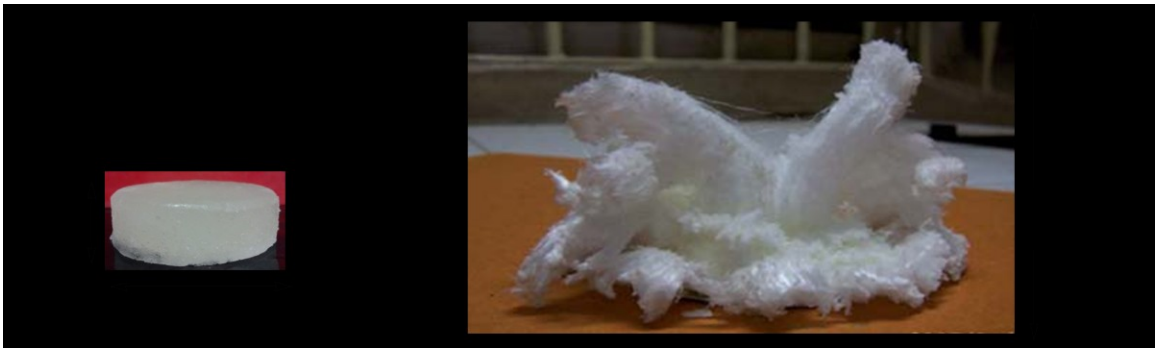

Fig. 3.2: Hair like crystal growth of $AnHNO_3$ (1a) from gel

Scheme: 3.4

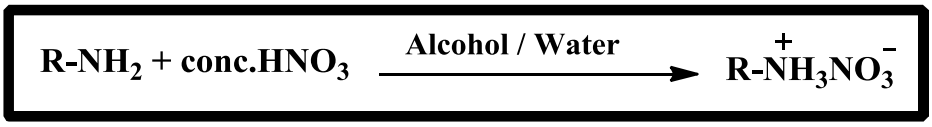

Where, R-NH_2 =

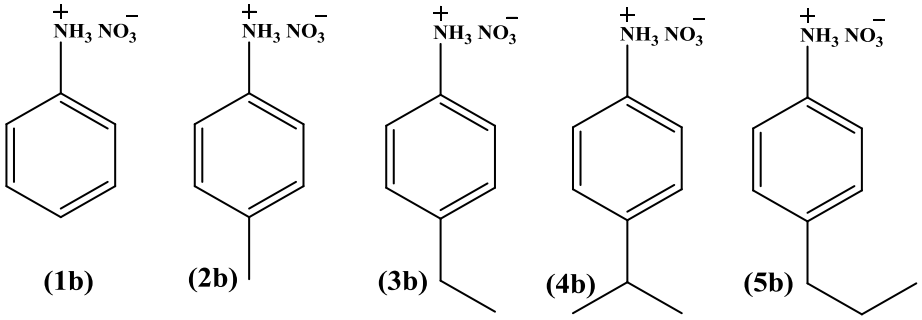

A series of anilinium nitrate derivatives were prepared by the dropwise addition of excess concentrated nitric acid (0.90 ml) to a solution of amines (0.50 ml) in 20 ml water. Slow evaporation of the aqueous solution at room temperature gave colourless crystals. Recrystallization was performed to increase purity using absolute ethanol which on slow evaporation gave good quality of single crystals.

Yield: 80-90 %

3.3 Result and Discussions

The grown crystals were characterized in order to study the structural and physical properties. Structural characterization involves identification of crystalline phase by single crystal X-ray diffraction analysis and Fourier transforms Infrared Spectroscopy. Electrical properties studied using Sawyer-Tower ferroelectric loop tracer. Thermal behavior of these crystals is studied by thermo gravimetry, differential thermal derivative thermo Gravimetry, differential scanning calorimetry, and variable temperature FT-IR and variable temperature single crystal X-ray diffraction.

3.3.1 FT-IR Spectra

The vibrational measurements for a series of nitrate salts were recorded in the range of 4000-400 cm^{-1}. Figure 3.3 shows the FT-IR spectra of gel hair compounds and sugar/needle crystals respectively at RT.

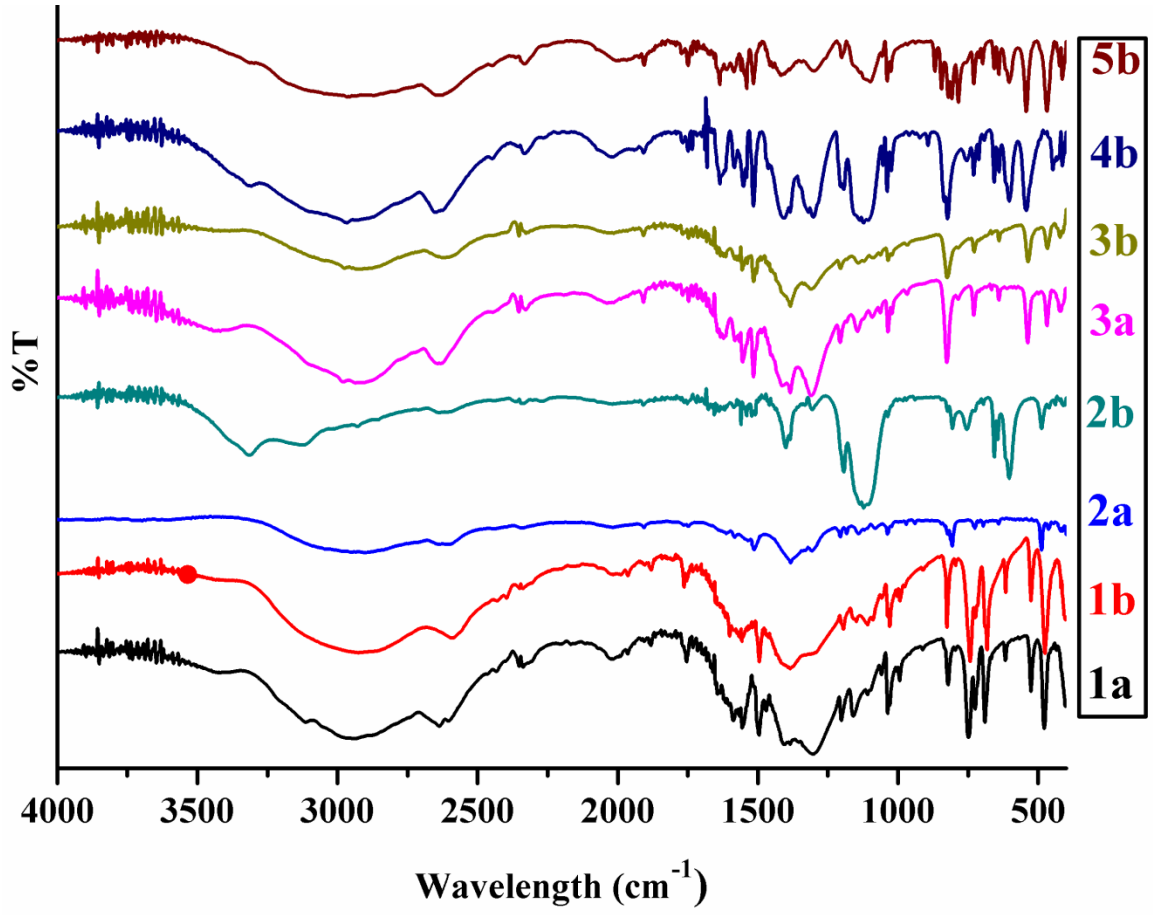

Fig. 3.3: FT-IR of compound 1a, 1b, 2a, 2b, 3a, 3b, 4b and 5b

Table 3.2: Wave-numbers (cm^{-1}) of the bands observed in FT-IR spectra of all compounds

1a	1b	2a	2b	3a	3b	4b	5b	Assignment
3117s	3140s	3130s	3124s	3112s	3109s	3105m	3131m	**Asym/ symm stretch (NH_3^+)**
2948bs	2922bs	2905bs	2928m	2985s	2977s	2968bs	2961bs	**C–H stretch**
				2924bs	2916bs			
2870m	2855m	2835m	2851w				2872bs	**N–H···O stretch**
2637m	2638m	2641m	2639m	2639s	2613s	2653s	2635s	
2605w	2588m	2603m	2602m			2627s		
2461w	2427w							
2430w	2429w	2441m	2437w	2443w	2439w	2448w	2444m	
2199w	2198w			2191w	2186w	2264w	2252w	
2157w	2148w						2201w	
2073w	2070w	2077w	2076w	2034m	2030m	2023s	2074w	**N–H···O stretch**
2021w	2024w	2015w	2023w					
1988w	1987m						2003s	**'Benzene finger'**
1964m	1963m						1925s	**'Benzene finger'**
1906w	1905w	1906m	1911m	1909m	1908m	1907m	1907s	**'Benzene finger'**
1881m	1881m					1842w	1869w	
						1808w	1830m	
1767m	1762s	1766w		1770w	1768m	1768m	1773m	
1754s	1754s	1747m	1752m	1744m	1747m	1749s	1748s	
1732w	1731w					1734m	1734m	
1696w						1701w	1701m	
1681w	1682w		1680m					
1669w	1667w					1670w	1673w	
1659w	1660w		1654m	1662m	1665m	1660w	1655w	

1644w		1644w			1643m	1636bs	1636s	**Ring stretch**
1614w	1616w	1613w	1612w	1619m		1616s	1616m	
1588s	1600s	1582m	1586m	1582m	1582m	1583s		**Asym def (NH_3^+)**
1565w	1565w			1568m			1570w	
1556m	1557s	1557w	1560m	1556s	1556s	1551vs	1560m	**Asym def (NH_3^+)**
1528w	1538w	1535w	1540m	1537w	1539w	1540s	1540vs	
1515w	1517w	1513s	1520m	1516s	1515s	1516s	1516vs	**Ring stretch**
1495vs	1494vs	1488w	1508m	1504w	1505s		1490m	**Ring stretch**
1469m	1470w			1488w	1486w	1464m	1472m	**Ring stretch**
1454w	1456w			1415s	1414w		1456m	**CH_2 sciss**
1407w			1400s			1407bs	1418bs	
1385w	1386w	1384bs	1384s	1383s	1384bs	1384s	1386w	**N–H···O in-plane def**
1340m	1349bs	1328w	1332w	1336w	1336w	1336s	1344w	**NO_3^- asym stretch**
						1322vs		
1302bs	1306s	1307m	1305m	1310vs	1310s	1305vs	1302s	**N–H···O in-plane def**
1202s	1194s	1206s	1195vs	1205s	1204s	1205s	1200s	**C–N stretch**
1160s	1159w	1183m,	1138bs	1181w	1183m	1194s		
		1140m	1123bs	1146m		1139bs		
1109w	1109m	1118w	1106bs	1121w	1120w	1125bs	1138s	**C–H in-plane def**
							1120bs	
1098w	1090m	1081m		1093w	1091m	1106bs	1099bs	**C–H in-plane def**
1058m	1059m			1062w	1063w	1054m	1058m	
1037s	1038s	1036s	1037m	1036s	1035s	1040s	1038vs	**NO_3^- asym stretch**
1030s	1029s	1022w	1020w	1022w	1021m	1023s	1025s	**NO_3^- asym stretch**
1005m	1003m	1002w	1002w					**6(A1) mode of benzene ring**
993s	994m		982w					**C–C and C–N stretch**

972w	977w	971m	970w	968w	967m	9611w	968w	**C–H out-of-plane def**
958w	959w	942m	939w				938w	**γ N–H···O**
913w	912w					920w		**γ N–H···O**
834w		835w	845m	825vs	826w	834vs	844s	**NO_3^- out-of-plane bend**
821vs	825vs	824m	824m	822w	822vs	822vs	821vs	**NO_3^- out-of-plane bend**
794w	794m	805vs	807s	786m	784m		784vs	**Symm ring breath**
750vs	741vs	732w	756s		743w	756s	756w	**In-plane ring def**
725vs	724s	725s	726w	729s	728s	730s	729s	**NO_3^- in-plane bend**
690vs	689m	697m	695w	711w	709w	711m	711m	**In-plane ring def**
		687vs				695m		
667w	667w	659w	658m	668w	667w	659s	657s	
617m	616s	640m	644m	604m	605m	642s	640s	**In-plane ring def**
			603vs				615s	
526vs	526vs			537vs	538vs	543vs	543vs	**Out-of-plane C–N bend**
478vs	475vs,	488s	488s	498s	468vs	446s	467vs	**Out-of-plane C–N bend**
	469m	463m	463m	468s				
447w	442w							
435w	434w		438w	420s	422s	431s	438w	
						412s	422s	

asym, asymmetric; bend, bending; breath, breathing; b, broad; def, deformation; m, medium; sciss, scissoring; stretch, stretching; symm, symmetric; s, strong; w, weak; v, very; vs, very strong

There is no distinguishable difference were observed in FT-IR of gel hair compounds and sugar/needle like compounds. Fundamental IR frequencies observed in all nitrate compounds in general, are also found in this analysis which confirms the nitrate group of the grown crystals [17].

3.3.1.1 Internal vibrations of NO^-_3 anions:

The IR modes observed for **1a**, **1b**, **2a**, **2b**, **3a**, **3b**, **4b** and **5b** for NO_3^- anion were listed in Table 3.2.

The NO_3^- anion having D_{3h} symmetry and contain distinct vibrational fundamental modes. The *anti-symmetric* stretching (υ_3) mode was generally observed at 1330 cm^{-1} while *symmetric* stretching (υ_1) mode at 1040 cm^{-1}. *Out-of-plane* bending (υ_2) mode was observed at 800 cm^{-1} while *in-plane* bending (υ_4) mode at 730 cm^{-1}.

Here *anti-symmetric* stretching (υ_3) mode observed in the range of 1028-1349 cm^{-1}. Two infrared bands of strong and medium/weak intensity observed at 1036-1040 cm^{-1} and 1020-1030 cm^{-1} respectively due to antisymmetric stretching vibrations of NO_3^- ion. This splitting corresponds to crystal field effect, as there are eight (Z = 8 for compounds **1a**, **1b** and **4b**) and four (Z = 4 for compounds **2a**, **2b**, **3a**, **3b** and **5b**) crystallographically equivalent ions in elementary unit cell [18].

Two bands in infrared spectrum are observed in the range of 834-845 cm^{-1} and 821-825 cm^{-1} in all compounds, originates from the bending (υ_2) type of vibrations of nitrate anions. In some of the compound first band is much weak (**1a**, **2a** and **2b**- weak, **1b**-absent) than others in which increment of alkyl group at para position of aniline (**3a**, **3b** and **5b**) generate strong band. Splitting of υ_2 mode into a *doublet* by addition of alkyl group (from methyl to propyl) may be due to lowering of symmetry of the NO_3^- ion from D_{3h} to C_{2v} or *Cs*. *In-plane*-bending (υ_4) mode observed in the range of 724-730 cm^{-1}.

3.3.1.2 The vibrations of anilinium cations:

Strong broad band for N-H ($-NH_3^+$ group) symmetric and asymmetric stretching vibrations were observed in the range of 3140-2600 cm^{-1} due to the continuous series of overlapping bands, combination bands and overtone bands. The aromatic C-H stretching vibrations were observed in the range of 2985-2916 cm^{-1}.The bands in the range of 2653-2613 cm^{-1} were assigned to the Fermi resonance of combination bands of (deformation and rocking modes) N-H of $-NH_3$ group.

The bands at 1644-1612 cm^{-1} and 1520-1470 cm^{-1} of weak/medium and strong respectively were attributed to ring stretching vibrations. Vibrations observed at 1194-1206 cm^{-1} assigned to C-N stretching vibration modes. The *in-plane* ring deformation, 8(B_1) modes observed at 756-741 and 711-687 cm^{-1}. Strong bands of *out-of-plane* bending vibration of C-N were observed in the range of 543-446 cm^{-1}.

Presence of strong bending and symmetric deformation modes of NH_3^+ group observed around 1588-1565cm^{-1} and 1560-1551cm^{-1} respectively confirms the proton transfer from nitric acid to amino group of aniline molecule.

Hydrogen bonding *in-plane* deformation (N–H---O) modes were observed at 1385-1305 cm^{-1}. Two bands in infrared spectrum are observed in the range of 2872-2835 cm^{-1} and 2074-2023 cm^{-1} as a medium and weak respectively assigned to the hydrogen bonding N–H---O stretching vibrations.

3.3.2 Raman Spectra

In this work, the internal modes observed in the Raman spectra from 400 to 1800 cm^{-1} were measured for gel hair compounds **1a**, **2a** and **3a** only (Figure 3.4; Table 3.3).

NO_3^- ion has D_{3h} symmetry and shows four vibrational fundamental modes [19]. For Raman spectra only three distinct vibrational Raman modes are observed at 1383, 1054 and 715 cm^{-1}.

A strong and a medium/weak mode appeared around 1034 and 722-729 cm^{-1} belonged to anti symmetric υ_1 (NO_3^- *asym stretch*) and the doubly degenerate υ_4 (NO_3^- *in-plane bend*) modes of NO_3^-, respectively. The bands for υ_3 mode were observed in the range from 1310 to 1442-1477 cm^{-1}. The Raman doublets 1034/1029 cm^{-1} was assigned to antisymmetric stretching vibrations of NO_3^- anions.

Weak band in range of 1540-1556 cm^{-1} indicates the $-NH_3$ symmetric bending mode. It is also seen in the Raman spectra, bands at 1178-1181 cm^{-1} and 462-532 cm^{-1} were assigned to the C-N *stretching* and *out-of-plane* bending modes respectively.

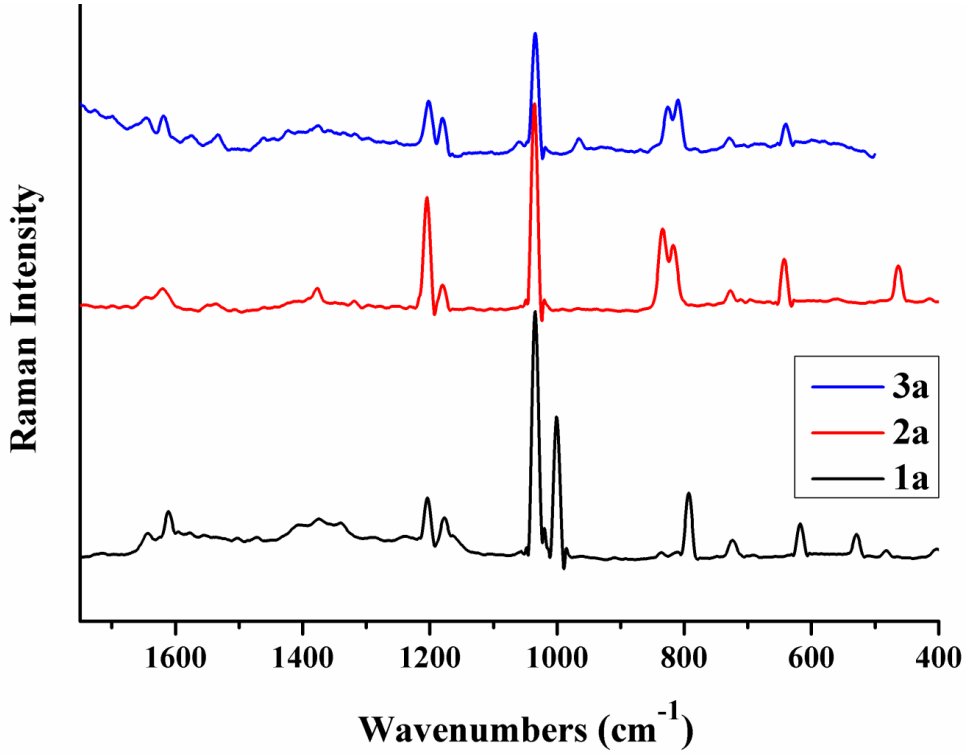

Fig. 3.4: Raman spectra of compound 1a, 2a, and 3a

Table 3.3: Relative intensities of the bands observed in the powder Raman spectra of 1a, 2a, and 3a

KNO_3	1a	2a	3a	Assignment
	1644m	1644w	1647w	
	1611m	1620m	1617w	**Ring stretch**
	1556w	1542w	1540w	**Asym def (NH_3)**
	1412w			
1354m	1342w	1377w	1377w	**NO_3^- asym stretch**
	1204s	1206s	1204s	**C–N stretch**
	1178m	1178m	1181m	**C–H in-plane def**
1050s	1034vs	1034vs	1034vs	**NO_3^- asym stretch**
	1020w	1019w	1018w	**NO_3^- asym stretch**
	999vs		967w	**C–C and C–N stretch**
	837w	834s	825s	**NO_3^- out-of-plane bend**
	794s	816s	809s	**Symm ring breath**
714m	722m	726m	729w	**NO_3^- in-plane bend**
	618m	644s	641m	**In-plane ring def**
	530m			**Out-of-plane C–N bend**
	484w	462s		**Out-of-plane C–N bend**

3.3.3 Elemental analyses:

The calculated elemental analyses were consistent with the observed formulae of nitrate salts.

Compound 1a: Anal. Calc. for $C_6H_8N_2O_3$: C, 46.15; H, 5.16; N, 17.94%; **Found:** C, 46.09; H, 5.12; N, 17.83%.

Compound 1b: Anal. Calc. for $C_6H_8N_2O_3$: C, 46.15; H, 5.16; N, 17.94%; **Found:** C, 45.96; H, 5.08; N, 17.90%.

Compound 2a: Anal. Calc. for $C_7H_{10}N_2O_3$: C, 49.41; H, 5.92; N, 16.46%; **Found:** C, 49.13; H, 5.89; N, 16.32%.

Compound 2b: Anal. Calc. for $C_7H_{10}N_2O_3$: C, 49.41; H, 5.92; N, 16.46%; **Found:** C, 49.02; H, 6.10; N, 16.12%.

Compound 3a: Anal. Calc. for $C_8H_{12}N_2O_3$: C, 52.17; H, 6.57; N, 15.21%. **Found:** C, 52.06; H, 6.51; N, 15.16%.

Compound 3b: Anal. Calc. for $C_8H_{12}N_2O_3$: C, 52.17; H, 6.57; N, 15.21%. **Found:** C, 51.89; H, 6.54; N, 15.09%.

Compound 4b: Anal. Calc. for $C_9H_{14}N_2O_3$: C, 54.53; H, 7.12; N, 14.13%; **Found:** C, 54.28; H, 7.08; N, 14.0%.

Compound 5b: **Anal. Calc. for** $C_9H_{14}N_2O_3$: C, 54.53; H, 7.12; N, 14.13%; **Found: C,** 54.49; H, 6.99; N, 14.19%.

3.3.4 ^{1}H NMR Spectra:

Formation of anilinium nitrate salt and its derivatives has been confirmed by ^{1}H NMR spectroscopy (Figure 3.5a-h). Anilinium nitrate (**1a**/**1b**) and its derivatives (**2a-3a/ 2b-5b)** showed broad signal between δ = 9.76 - 9.97 respectively for three proton due to -NH_3^+ moiety. Five aromatic C-H protons signals of **1a** and **1b** observed between δ = 7.34 - 7.50 while all other derivatives with four aromatic C-H protons showed signals at range of δ = 7.21 - 7.37. Signals for –CH_3 group in **2a-3a/ 2b-5b** observed in the range of δ = 0.85 – 2.32 (**2a**/**2b**: δ 2.32, **3a**/**3b**: δ 1.13-1.18, **4b**: δ 1.18 and **5b**: δ 0.85-0.89), depends on the position of it. In case of compound **3a** and **3b**, –CH_2 protons showed quartet in the range of δ = 2.59-2.67. In 4-*iso* propyl anilinium nitrate (**4b**) peaks at δ = 2.87-2.94 and δ = 1.18 are due to the one and six proton of -CH and –CH_3 respectively. In case of 4-propyl anilinium nitrate (**5b**) peaks around δ = 2.55-2.59 and δ = 1.53-1.62 indicate the methylene –CH_2 group protons respectively. The details of ^{1}H NMR spectra for all these compounds are tabulated in Table 3.4.

Table 3.4: Chemical shifts of ^{1}H NMR spectra of compounds 1a, 1b, 2a, 2b, 3a, 3b, 4b and 5b

Compound	Gel hair (δ value) ^{1}H NMR (d_6-DMSO) J coupling in Hz	Sugar/ Needle (δ value) ^{1}H NMR (d_6-DMSO) J coupling in Hz
AnHNO$_3$	**1a**:δ 9.79(br s 3H, NH_3^+), 7.50 (tt 2H, J = 6.8 and 8.1), 7.41 (tt 1H, J = 7.6 and 7.2), 7.34 (dt 2H, J = 6.9)	**1b**: δ 9.89 (br s 3H, NH_3^+), 7.50 (tt, 2H, J = 6.8 and 8.1), 7.41 (tt, 1H, J = 7.6 and 7.2), 7.34 (dt, 2H, J = 6.9).
4MeAnHNO$_3$	**2b**:δ 9.83(br s 3H,NH_3^+), 7.30 (d 2H, J = 8.0), 7.23 (d 2H, J = 8.0), 2.32 (s 3H)	**2b**: δ 9.96 (br s 3H, NH_3^+), 7.30 (d 2H, J = 8.4), 7.25 (d 2H, J = 8.4), 2.32 (s 3H).
4EtAnHNO$_3$	**3a**:δ 9.87(br s 3H, NH_3^+), 7.30-7.35 (d 2H, J = 7.26), 7.20-7.27 (d 2H, J = 7.24), 2.59-2.66(q, 2H, J = 7.59), 1.13-1.18 (t, 3H, J = 7.6).	**3b**: δ 9.76 (br s 3H, NH_3^+), 7.31-7.34 (dd 2H, J = 3.6 and 4.8), 7.21-7.25 (dt 2H, J = 6.4 and 7.6), 2.59-2.67(q, 2H, J = 7.6), 1.14-1.18 (t, 3H, J = 7.6).
4*i*PrAnHNO$_3$		**4b**: δ 9.97 (br s 3H, NH_3^+), 7.37 (d 2H, J = 8.4), 7.28 (dd 2H, J = 2.0 and 1.6), 2.87-2.94(dt, 1H, J = 6.8 and 7.2), 1.18 (d, 6H, J = 7.2).
4*n*PrAnHNO$_3$		**5b**: δ 9.87 (br s 3H, NH_3^+), 7.31 (d 2H, J = 8.4), 7.25 (dt 2H, J = 2 and 6.4), 2.55-2.59(t, 2H, J = 7.2 and 8.0), 1.53-1.62(qd 2H, J = 7.6 and 7.2), 0.85-0.89 (t, 3H, J = 7.2).

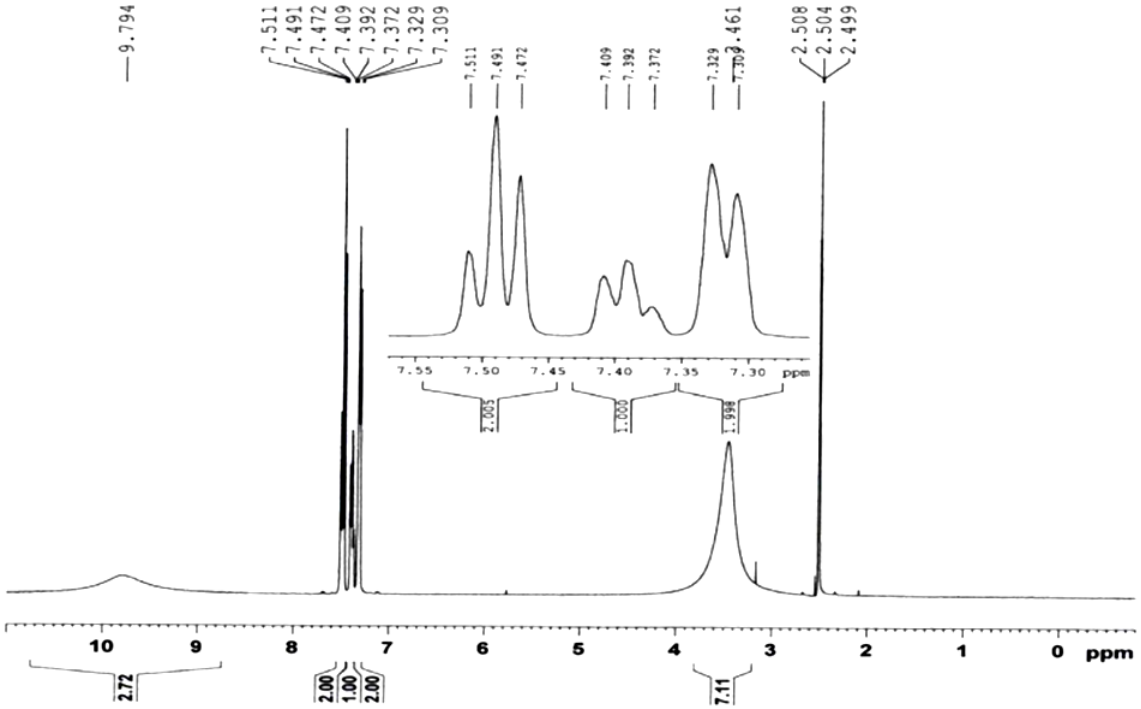

Fig. 3.5 (a): ^{1}H NMR spectra of anilinium nitrate (1a)

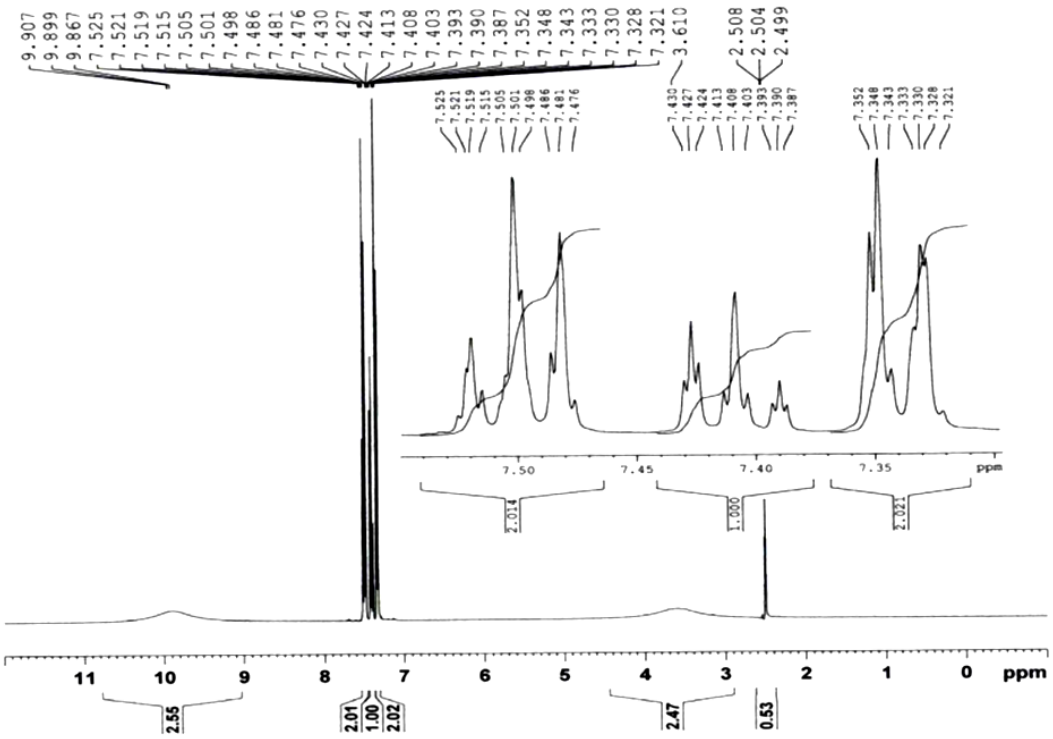

Fig. 3.5 (b): ^{1}H NMR spectra of anilinium nitrate (1b).

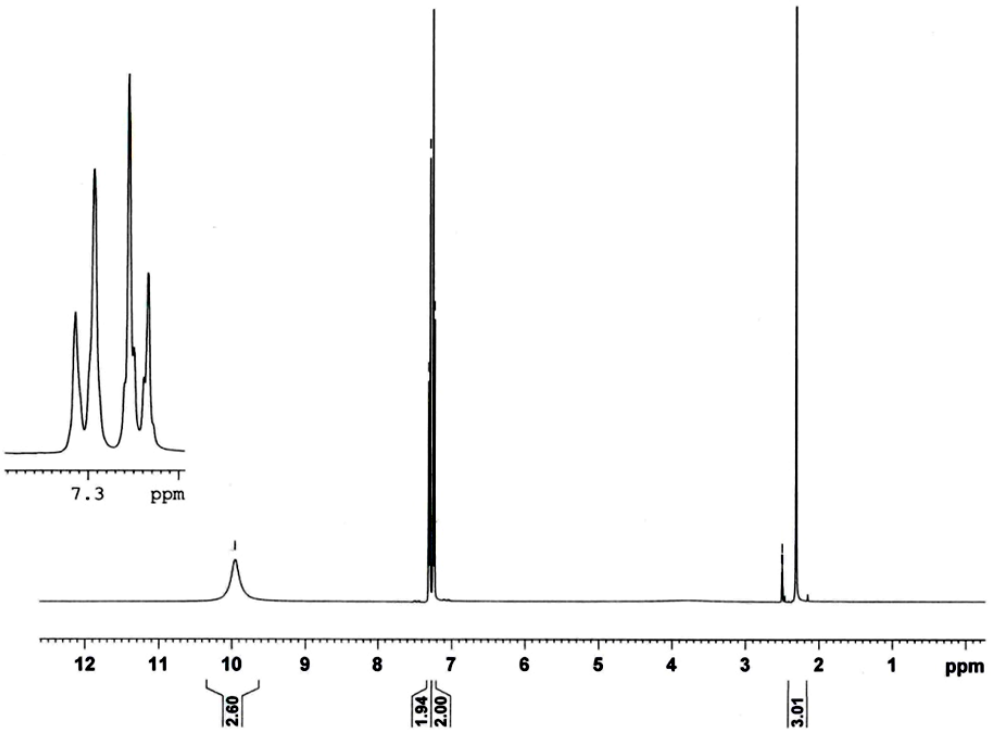

Fig. 3.5 (c): ^{1}H NMR spectra of 4-methyl anilinium nitrate (2a).

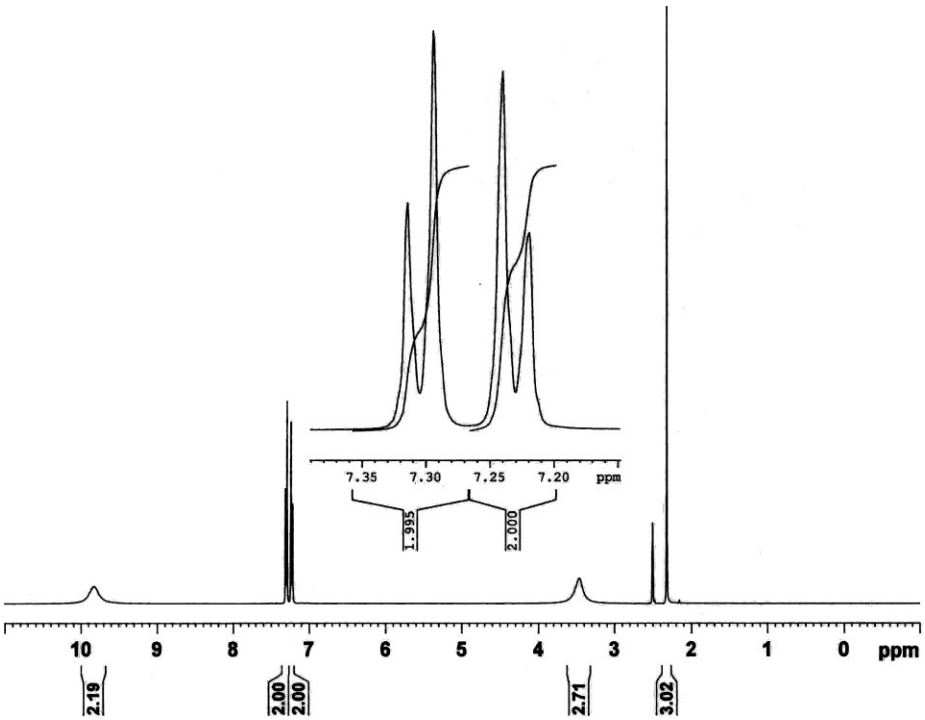

Fig. 3.5 (d): ^{1}H NMR spectra of 4-methyl anilinium nitrate (2b).

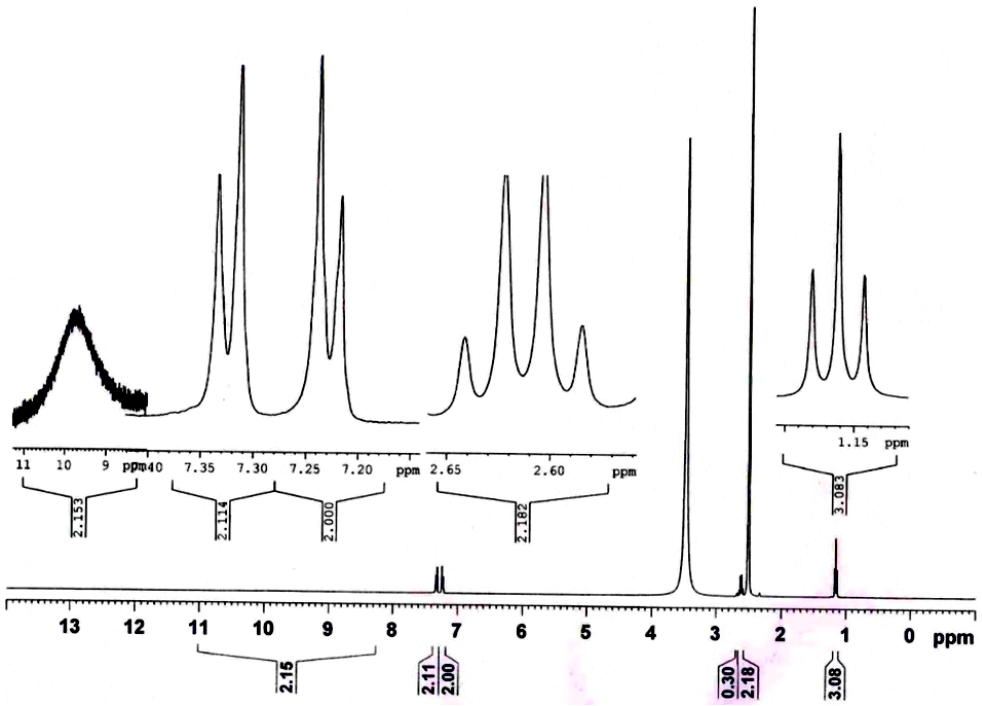

Fig. 3.5 (e): ^{1}H NMR spectra of 4-ethyl anilinium nitrate (3a)

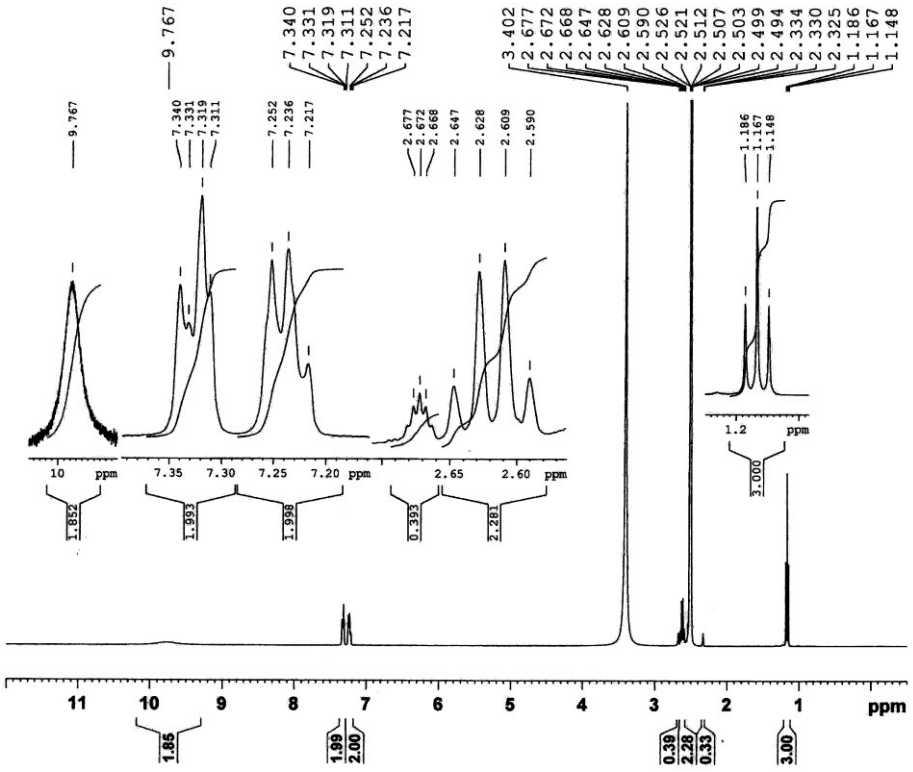

Fig. 3.5 (f): ^{1}H NMR spectra of 4-ethyl anilinium nitrate (3b)

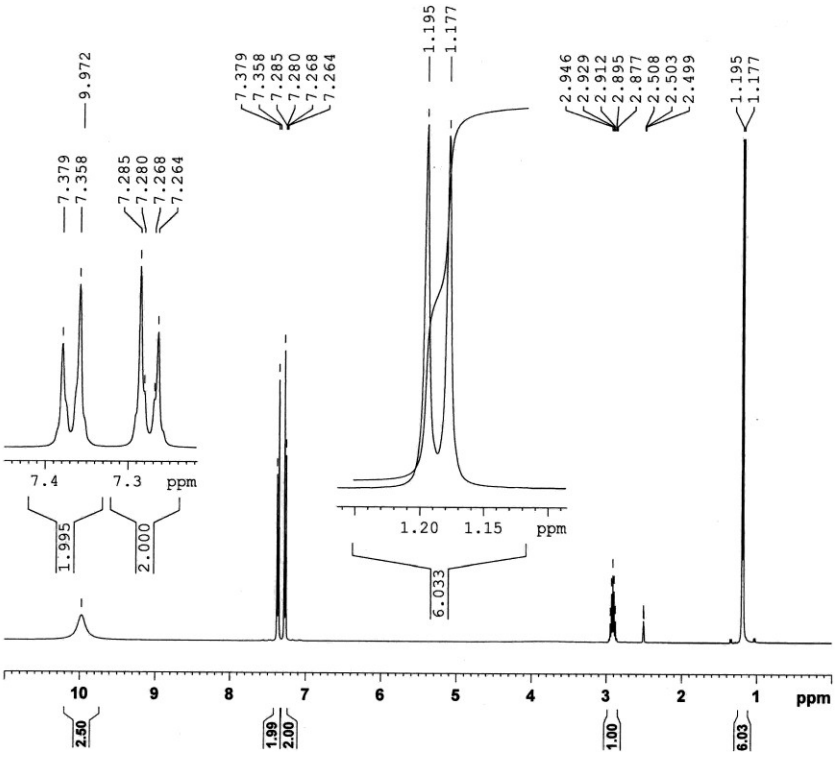

Fig. 3.5 (g): ^{1}H NMR spectra of 4-iso Propyl anilinium nitrate (4b)

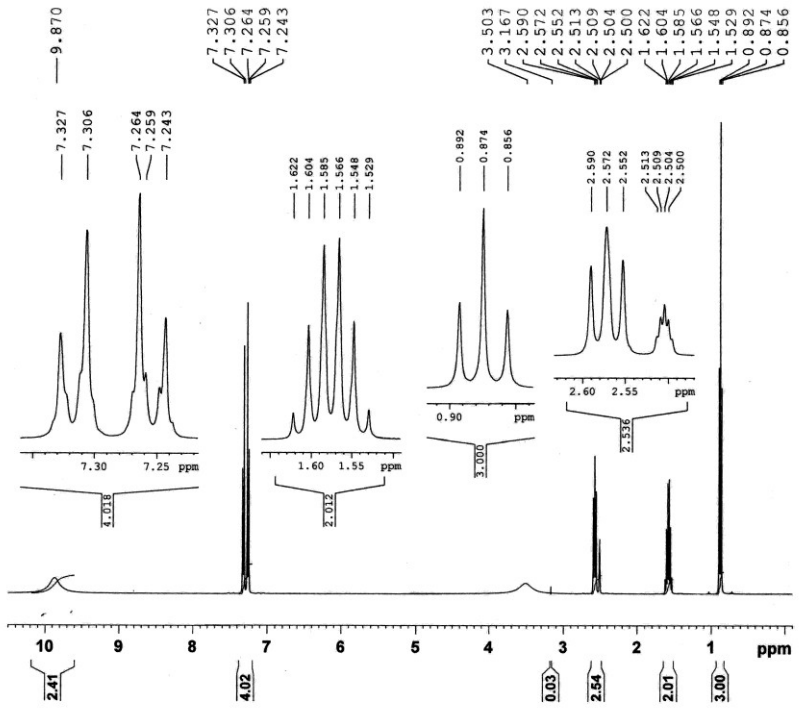

Fig. 3.5 (h): ^{1}H NMR spectra of 4-Propyl anilinium nitrate (5b)

3.4 Thermal Studies

3.4.1 TG-DTA:

Thermo-gravimetric studies were carried out for the all compounds **1a-3a** and **1b-3b** in nitrogen atmosphere in the 300-850 K temperature range (Figure 3.6). The single step decomposition patterns of all compounds are quite similar and can be generalized by saying that decomposition step is accompanied by the gradual loss of aniline moiety with mass loss of HNO_3 moiety.

The aniline.HNO_3 moiety from all compounds decomposes gradually i.e. Obsd. 100 %, Calcd. 100% in the range of 393-498 K for **1a**, 390-498 K for **1b**, 388-559 K for **2a**, 398-558 K for **2b**, 380-554 K for **3a** and 383-556 K for **3b**.

The DTA curves for all compounds **1a** (389.5 K), **1b** (384 K), **2a** (376 K) and **2b** (374.7 K) showed the solid-solid phase transition. Compound **3a** and **3b** showing two endothermic peaks at 347 K and 419.2 K for **3a** while 347 K and 417 K for **3b** corresponds to solid-solid and solid liquid phase transitions respectively. Exothermic effect was observed at 488 K for **1a**, 491 K for **1b**, 517.8 K for **2a**, 515.9 K for **2b**, 456.1 K for **3a** and 457.5 K for **3b**.

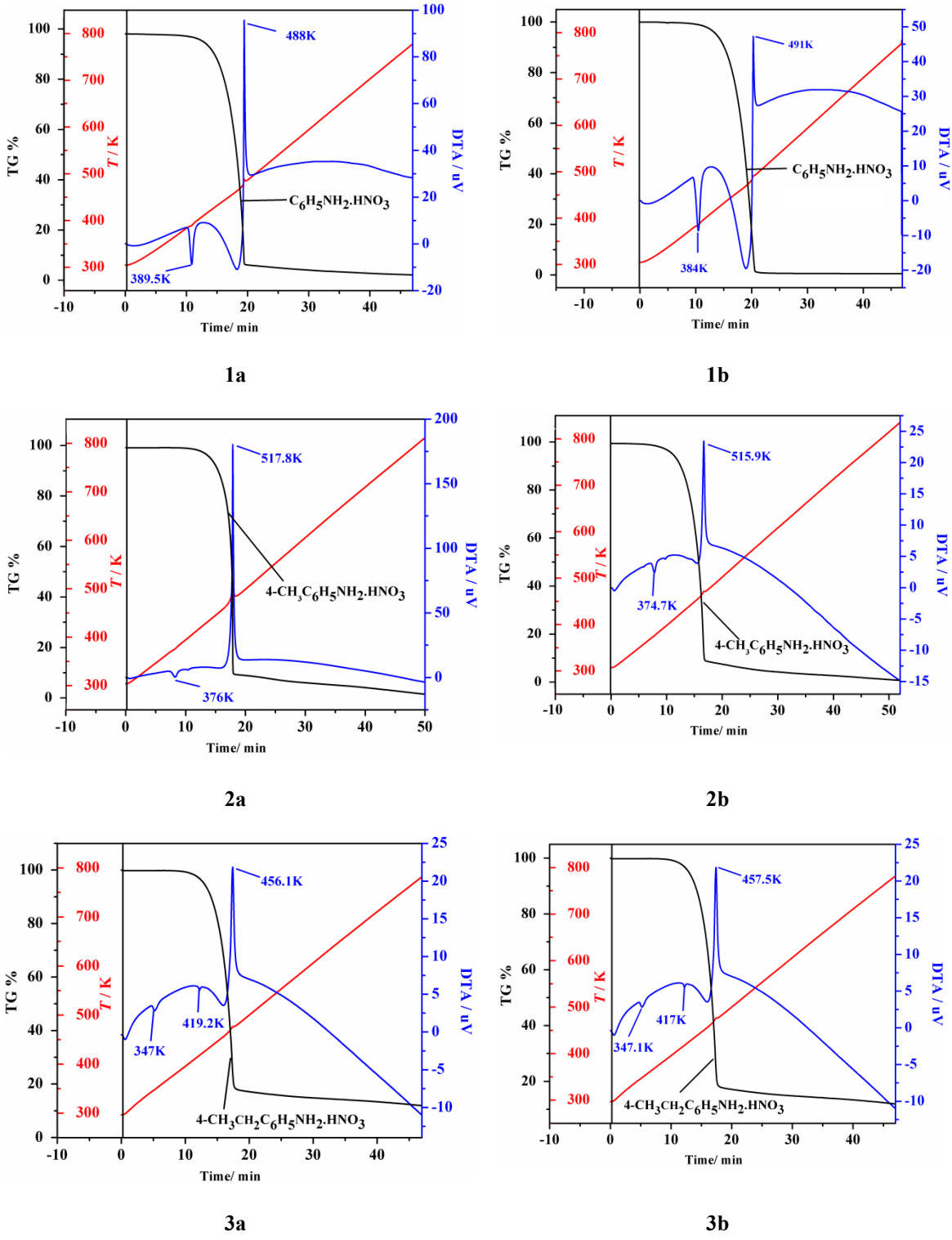

Fig. 3.6: TG-DTA of compound 1a, 1b, 2a, 2b, 3a and 3b

3.4.2 DSC:

To confirm degradation pathways and exothermic behavior of DTA we carried out DSC on all gel hair compounds (**1a-3a**) and sugar/needle compounds (**1b-5b**) from 298K to their degradation temperature (Figure 3.7). DSC studies on compounds showed presence of reversible solid-solid phase transition. These solid-solid phase transitions may be related to the structural reorientation which changes with temperature. Few of them exhibited thermal behavior with a sharp melting point on heating and subsequent crystallization on cooling that were reproducible throughout all heating and cooling cycles. This shows the reversibility of this order–disorder transition. Thermodynamic data for these compounds are shown in Table 3.5.

The thermodynamic values for compound **1a** and **1b** obtained for the endothermic phase transition during heating are 117.03ºC (-40.16 Jg^{-1}) and 109.76ºC (-46.71 Jg^{-1}) while an exothermic transition at 64.79ºC (49.56 Jg^{-1}) and 88.62 ºC (46.89 Jg^{-1}) during cooling, as shown in Figure 3.7. Compound **2a** and **2b** showed three endothermic phase transitions during heating, out of which two belongs to solid-solid phase transition [80.97 ºC (-14.22Jg^{-1}) and 98.95 ºC (-11.76 Jg^{-1}) for **2a**; and 79.59 ºC (-20.89 Jg^{-1}) and 94.98 ºC (15.13 Jg^{-1})] and one belong to melting transition [123.65 ºC (-6.43 Jg^{-1}) and 123.12 ºC (-6.43 Jg^{-1})]. During cooling, crystallization transition from the melt gave single exothermic phase transition at 119.84 ºC (5.53 Jg^{-1}) for **2a** and 120.39 ºC (6.16 Jg^{-1}) for **2b.**

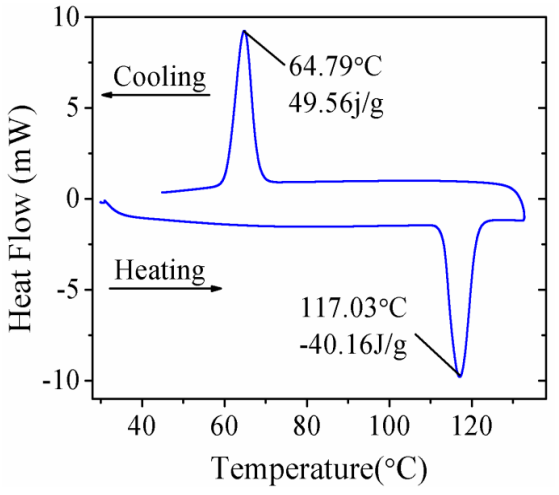

1a

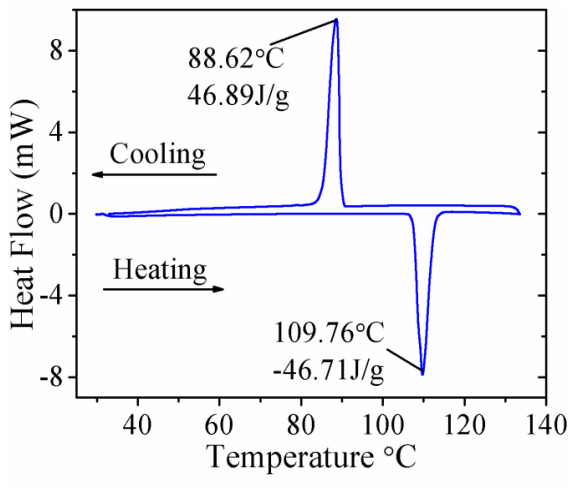

1b

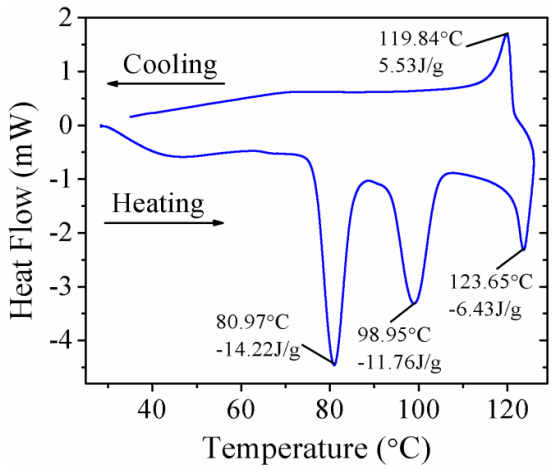

2a

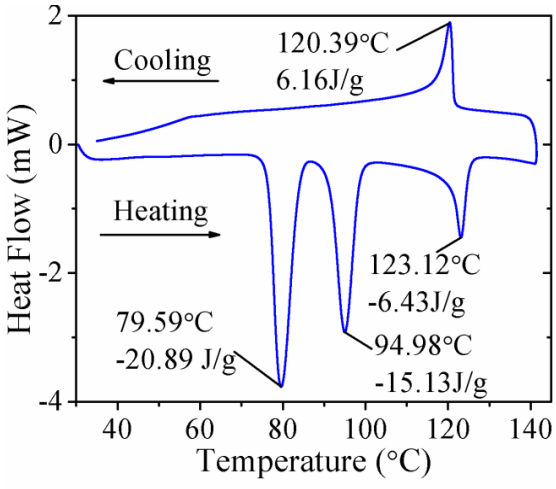

2b

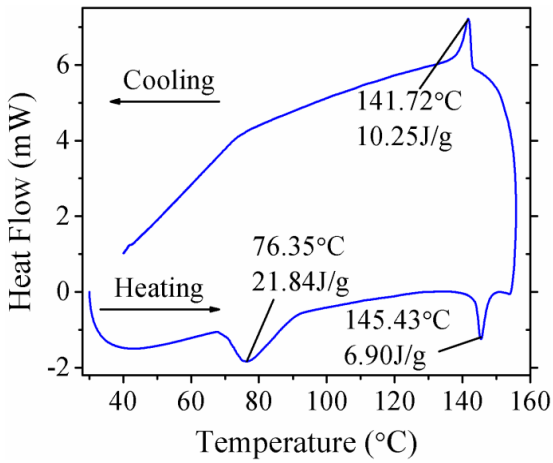

3a

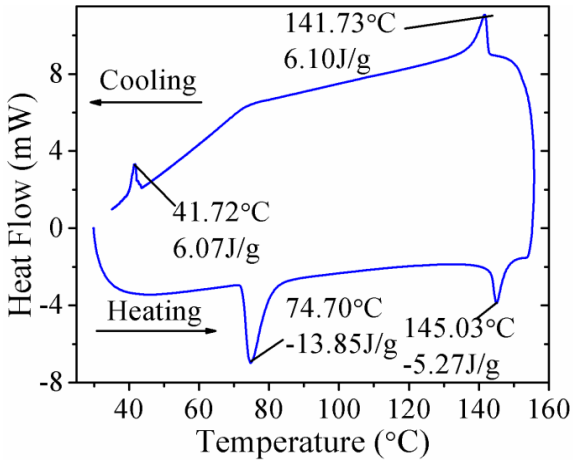

3b

Fig. 3.7: DSC chart of compound 1a, 1b, 2a, 2b, 3a and 3b at different temperatures

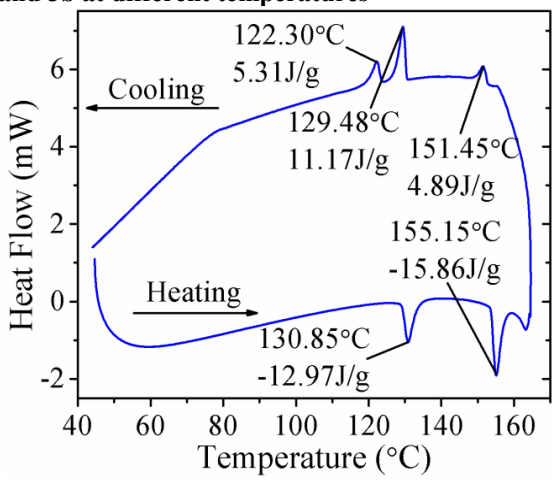

5b

Fig. 3.7: DSC chart of compound 5b at different temperatures

Table 3.5: DSC chart of compound 1a, 1b, 2a, 2b, 3a, 3b, 4b and 5b at different temperatures

Compounds	Phase Transition			
	Heating		Cooling	
	Temperature [ºC]	Enthalpy[J/g]	Temperature [ºC]	Enthalpy[J/g]
1a	117.03	-40.16	64.79	49.56
1b	109.76	-46.71	88.62	46.89
2a	80.97	-14.22	119.84	5.53
	98.95	-11.76		
	123.65	-6.43		
2b	79.59	-20.89	120.39	6.16
	94.98	-15.13		
	123.12	-6.43		
3a	76.35	-21.84	141.72	10.25
	145.43	-6.90		
3b	74.70	-13.85	141.73	6.10
	145.03	-5.27	41.72	6.07
4b	No transition observed.			
5b	130.85	-12.97	151.45	4.89
	155.15	-15.86	129.48	11.17
			122.30	5.31

Interestingly DSC studied on compounds **3a** and **3b**, found different observation than previous compounds. Compound **3a** is showing two endothermic peaks [76.35 ºC (-21.84 Jg^{-1}) and 145.43ºC (-6.90 Jg^{-1})] during heating and one exothermic peak [141.72 ºC (10.25 Jg^{-1})] during cooling, while compound **3b** showing two endothermic peaks [74.70 ºC (-13.85 Jg^{-1}) and 145.03 ºC (-5.27 Jg^{-1})] during heating and two exothermic peaks

[141.73 ºC (6.10 Jg^{-1}) and 41.72 ºC (6.07 Jg^{-1})] during cooling. In case of **3a** and **3b**, during heating in which first peak is of characteristic for solid-solid phase transition and second peak characteristic for solid liquid phase transitions. Whereas, during cooling **3a** showed one exothermic transition characteristic for liquid-solid phase transitions (crystallization transition) and **3b** showed two endothermic transitions characteristic for liquid-solid phase transitions (crystallization transition) and solid-solid phase transition.

Compound **4b** does not showed any phase transition. Surprisingly compound **5b** showed much different DSC measurements behavior than previous compounds. It showed two endothermic peaks [130.85 ºC (-12.97 Jg^{-1}) and 155.15 ºC (-15.86 Jg^{-1})] during heating characteristic for solid-solid phase transition while three exothermic transitions [151.45ºC (4.89 Jg^{-1}); 129.48 ºC (11.17 Jg^{-1}) and 122.30 ºC (5.31 Jg^{-1})]. Endothermic and exothermic transitions are due to characteristic for solid-solid phase transitions. No solid liquid phase transition i.e. melting was observed.

3.5 Electric Properties

Ferroelectric loop (PE, polarization versus electricity) measurements were performed on all samples in pellets to check the polarization hysteresis. We have found excellent ferroelectricity in a hair like crystal of compounds **1a** and **3a**: large spontaneous polarization, switchable with a relatively small electric field at room temperature. Polarization hysteresis was not observed for crystalline compounds **1b-3b**. The ferroelectricity loop measurements (PE loop) on a compounds **1a** and **3a** are depicted in Figure 3.8a and 3.8b.

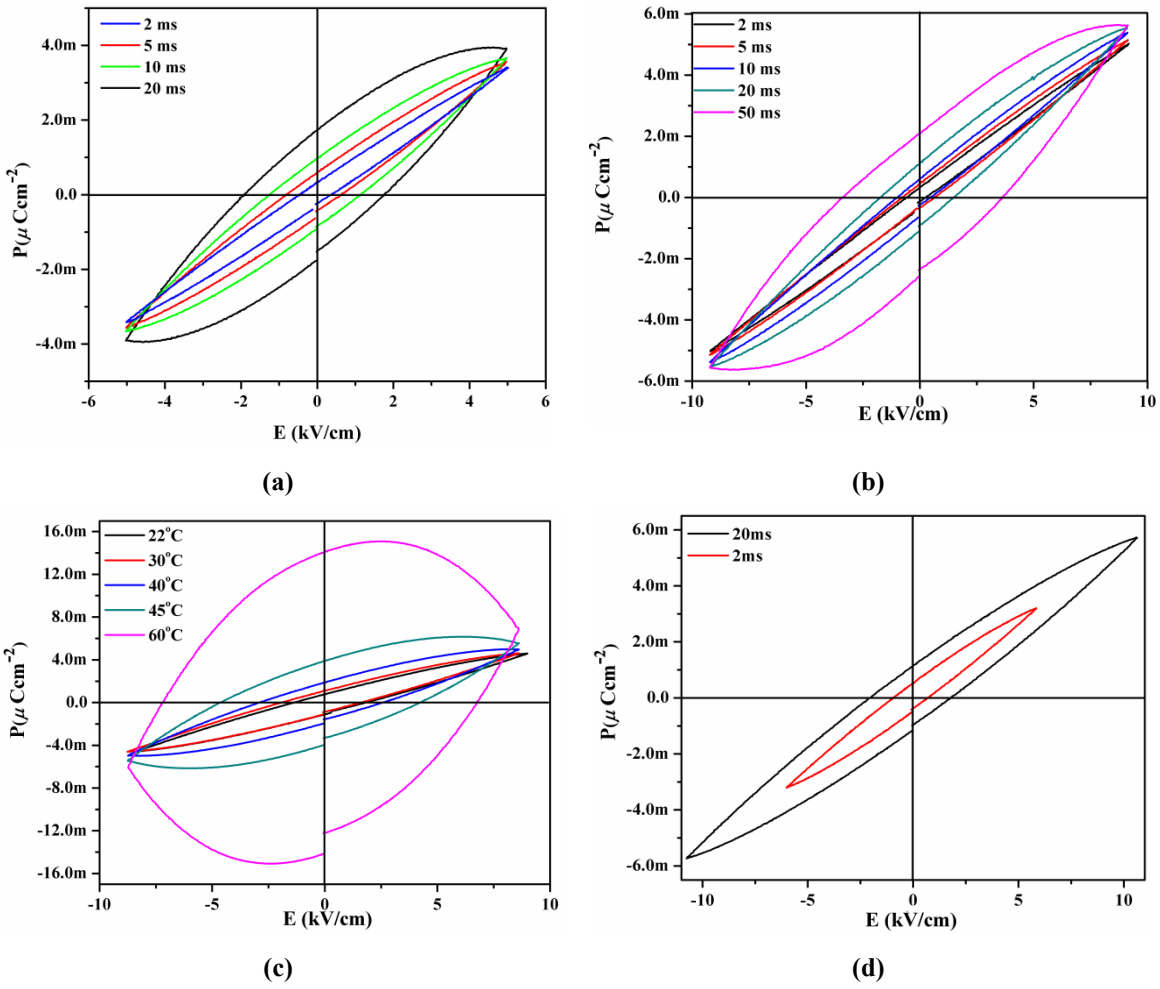

Fig. 3.8: (a) PE Loop measurement of $AnHNO_3$ hairs; (b) PE Loop measurement of 4-$EtAnHNO_3$ hairs; (c) PE Loop measurement of 4-$EtAnHNO_3$ hairs with temp.; (d) PE Loop measurement of 4-$EtAnHNO_3$ hairs with re-temp

Hysteresis measurements gave a well-defined nearly rectangular loop for compound **1a** (Figure 3.8a) with the maximum field of 1.94kVcm^{-1}. Depending on the a.c. frequency

(500 Hz to 50 Hz), coercive field *E*c typically ranges from 0.48 to 1.94 $kVcm^{-1}$ while remnant polarization *P*r ranges from 0.31 to 1.71 μCcm^{-2} at 300 K.

With change in a.c. frequency from 500 to 20 Hz, compound **3a** at 300 K showed hysteresis loop with coercive field *E*c observed in the range of 0.55 to 3.37$kVcm^{-1}$ while remnant polarization *P*r ranges from 0.33 to 2.09μCcm^{-2}.

DSC measurements on compound **3a** showed reversible phase transition temperature at 76.35ºC. Hence we tried variable temperature PE loop measurement at 50 Hz on compound **3a** at its phase transition temperature. As temperature increased from 295K to 333K, leakage current increased dramatically which is a general phenomenon in molecular ferroelectrics due to presence of small dielectric constants. With increase in temperature from 295K to 318K, coercive field *E*c also increased and falls in the range of 1.33 to 4.62 $kVcm^{-1}$. Crystal structure suggest that at phase transition temperature molecular rearrangements (symmetry breaking) took place and it crystallized into nonpolar space group which might showed paraelectric property. Hence electric measurements observation matches with crystal structure data.

On cooling to room temperature, hysteresis measurements were performed on compound **3a**. It showed a well-defined rectangular loop suggesting the phase transition is reversible in nature. Crystal structure also showed similar arrangement at room temperature.

Hence we obtained room temperature 'Molecular Ferroelectric'.

3.6 Optical Properties

3.6.1 CD Spectra

The result of circular dichroism (CD) spectrum measurements on single crystals of compound **3P** and **3M** in *nujol* further confirm the optical activity [20] and enantiomeric nature of complexes shown in the Figure 3.9.

Compound **3P** isomer exhibits a negative dichroic signal at 209 nm, 256 nm, 317 nm, 373nm, 440 nm, 506nm, 649 nm, 690 and positive dichroic signal at 270 nm, 346nm, 500 nm while compound **3M** isomer shows Cotton effect with opposite sign at the same wavelength (Figure 3.9). Solid-state CD measurements for the bulk materials are CD-silent, indicating two isomers in nearly 1: 1 ratio. Each individual single crystal was optically active. The static process produced the expected statistically equal number of **3P** (left-handed) and **3M** (right-handed) crystals during crystallization.

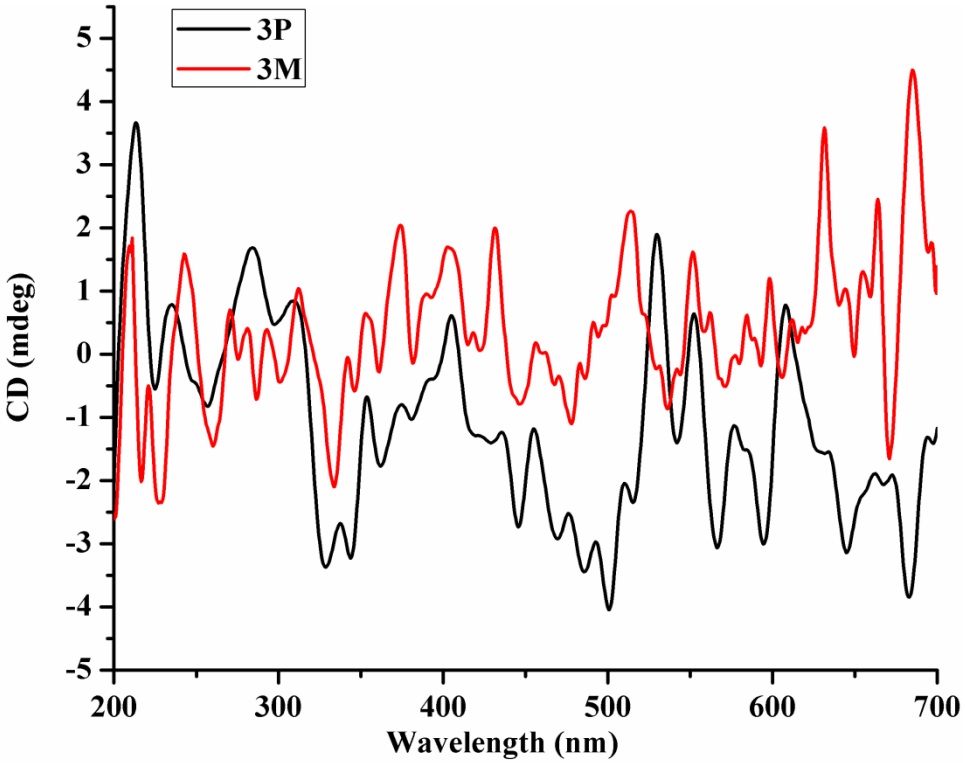

Fig. 3.9: Solid CD spectra of compound 3P and 3M in nujol

3.7 Crystal structure

3.7.1 Single Crystal X-ray Diffraction

The molecular structure of **1b, 2b, 3b-M, 3b-P, 4b** and **5b** are shown in Figure 3.10 (a-f). The molecular structure of **1a** and **3a** are shown in Figure 3.11 a-b. The selected bond lengths, angles and hydrogen bonds of the title compound are listed in Table 3.9, 3.10, 3.11 and 3.12.

Table 3.6: Crystal structure and refinement parameters for 1b, 2b, 3b-M, 3b-P, 4b and 5b

Identification code	1b	2b	3b-M	3b-P	4b	5b
Empirical formula	$C_6H_8N_2O_3$	$C_7H_{10}N_2O_3$	$C_8H_{12}N_2O_3$	$C_8H_{12}N_2O_3$	$C_9H_{14}N_2O_3$	$C_9H_{14}N_2O_3$
Formula weight	156.14	170.17	184.20	184.20	198.22	198.22
Temperature/K	293(2)	150(2)	293(2)	150(2)	293.0	293(2)
Crystal system	orthorhombic	monoclinic	orthorhombic	orthorhombic	orthorhombic	monoclinic
Space group	*Pbca*	$P2_1/n$	$P2_12_12_1$	$P2_12_12_1$	*Pbca*	$P2_1/c$
a/Å	10.158(2)	5.6677(5)	5.54536(14)	5.597(3)	9.7381(2)	5.46121(19)
b/Å	9.277(2)	8.5764(8)	**19.4934(5)**	**9.129(5)**	10.9519(3)	19.5309(7)
c/Å	16.177(3)	17.6199(14)	**9.0081(2)**	**19.608(10)**	20.1210(6)	10.0581(4)
α/°	90.00	90.00	90.00	90.00	90	90.00
β/°	90.00	99.026(5)	90.00	90.00	90	103.031(3)
γ/°	90.00	90.00	90.00	90.00	90	90.00
Volume/Å^3	1524.5(5)	845.87(13)	973.76(4)	1002.0(9)	2145.93(10)	1045.19(7)
Z	8	4	4	4	8	4
ρ_{calc}mg/mm^3	1.361	1.336	1.256	1.221	1.2270	1.260
m/mm^{-1}	0.111	0.106	0.815	0.094	0.093	0.795
F(000)	656.0	360.0	392.0	392.0	848.5	424.0
Radiation	0.71073	0.71073	1.5418	0.71073	0.7107	1.54184
Reflections collected	13258	3814	3649	5726	11955	3485
Independent reflections	2025 [R_{int} =0.0295, R_{sigma} = 0.0230]	1852 [R_{int} =0.0445, R_{sigma} = 0.0727]	1895 [R_{int} =0.0150, R_{sigma} = 0.0192]	1768 [R_{int} =0.1558, R_{sigma} = 0.0989]	2336 [R_{int} =0.0297, R_{sigma} = 0.0165]	2033 [R_{int} =0.0179, R_{sigma} = 0.0280]
Data/restraints/parameters	2025/0/133	1852/0/149	1895/0/120	1768/0/131	2336/0/156	2033/0/130
Goodness-of-fit on F^2	0.729	0.958	1.055	0.950	1.555	1.014
Final R indexes [I>=2σ (I)]	R_1 = 0.0379, wR_2 = 0.0854	R_1 = 0.0497, wR_2 = 0.1093	R_1 = 0.0462, wR_2 = 0.1355	R_1 = 0.0566, wR_2 = 0.1311	R_1 = 0.0615, wR_2 = N/A	R_1 = 0.0514, wR_2 = 0.1626
Final R indexes [all data]	R_1 = 0.0758, wR_2 = 0.1107	R_1 = 0.1006, wR_2 = 0.1345	R_1 = 0.0476, wR_2 = 0.1376	R_1 = 0.0831, wR_2 = 0.1547	R_1 = 0.0741, wR_2 = 0.2181	R_1 = 0.0579, wR_2 = 0.1709
Flack parameter			-0.1(4)	3(3)		

Table 3.7: Crystal structure and refinement parameters for 1a and 3a

Identification code	1a	3a
Empirical formula	$C_6H_8N_2O_3$	$C_8H_{12}N_2O_3$
Formula weight	156.14	184.20
Temperature/K	293(2)	293(2)
Crystal system	orthorhombic	orthorhombic
Space group	*Pbca*	$P2_12_12_1$
a/Å	10.1448(8)	5.559(2)
b/Å	9.2781(15)	9.010(6)
c/Å	16.147(2)	19.472(9)
α/°	90	90.00
β/°	90	90.00
γ/°	90	90.00
Volume/Å^3	1519.9(3)	975.3(9)
Z	8	4
ρ_{calc}mg/mm^3	1.3646	1.254
m/mm^{-1}	0.949	0.097
F(000)	658.6	392.0
Radiation	Cu Kα (λ = 1.54184)	MoKα (λ = 0.71073)
Reflections collected	1137	6173
Independent reflections	583 [R_{int} = 0.0162, R_{sigma} = 0.0368]	1944 [R_{int} = 0.1787, R_{sigma} = 0.1870]
Data /restraints/ parameters	583/0/101	1944/0/121
Goodness-of-fit on F^2	0.973	0.989
Final R indexes [I>=2σ (I)]	R_1 = 0.0356, R_2 = 0.0864	R_1 =0.0717, wR_2=0.1447
Final R indexes [all data]	R_1 = 0.0573, wR_2= 0.0987	R_1 = 0.2270, wR_2 = 0.2153
Flack parameter		-6(5)

3.7.1:1 Sugar/needle like crystals (1b-5b)

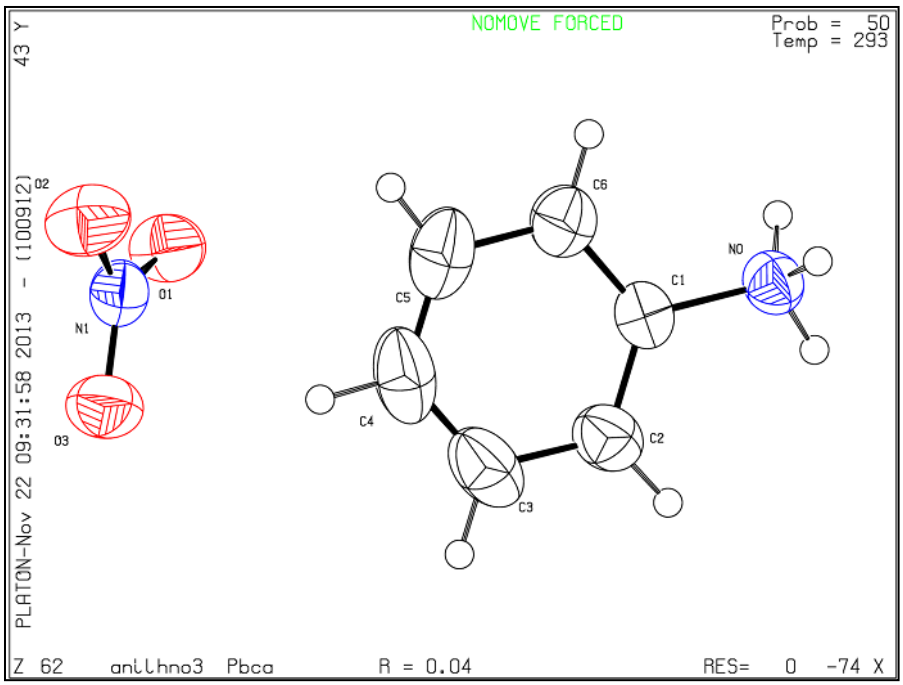

(a)

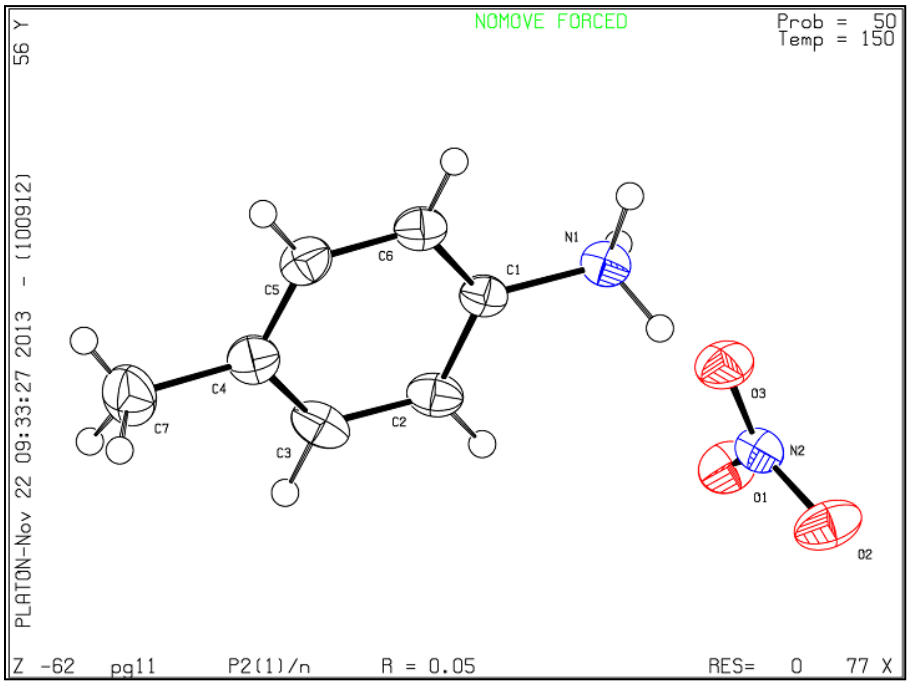

(b)

Fig. 3.10: Molecular view of compounds 1b (a) and 2b (b) having thermal ellipsoids are drawn at the 50% probability level

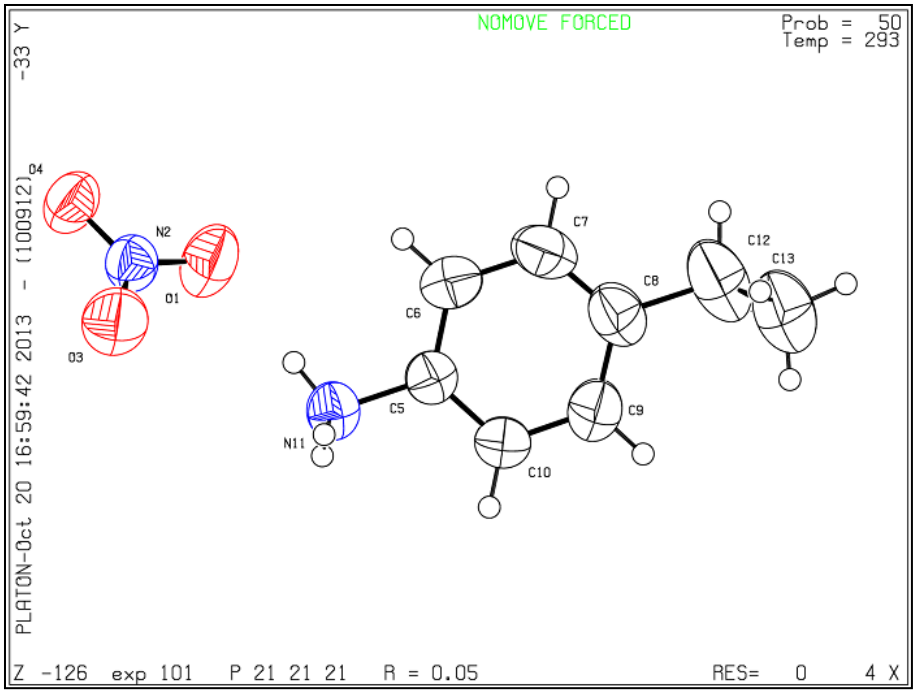

(c)

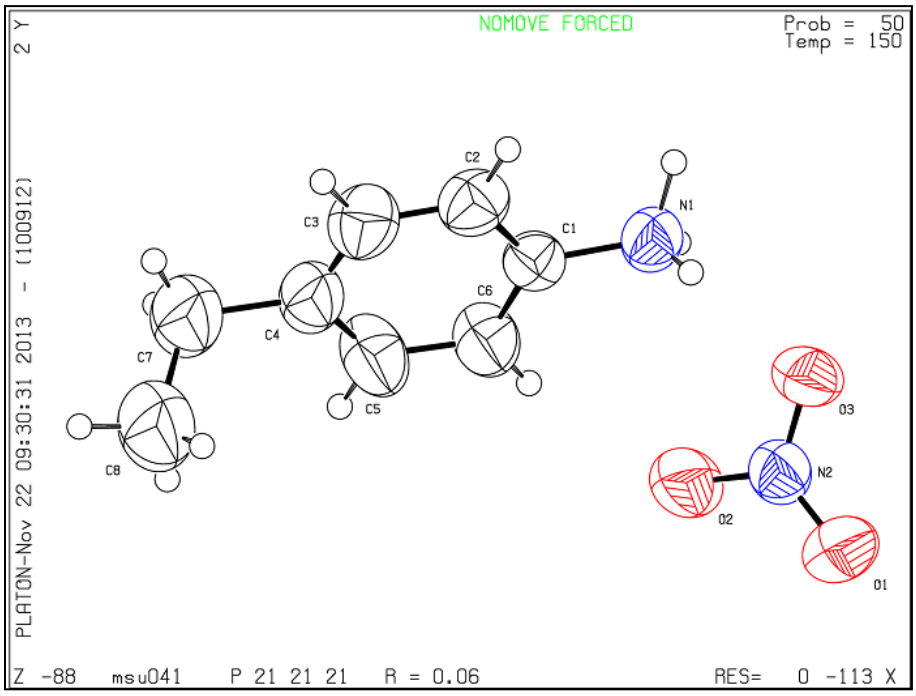

(d)

Fig. 3.10: Molecular view of compounds 3b-M (c) and 3b-P (d) having thermal ellipsoids are drawn at the 50% probability level

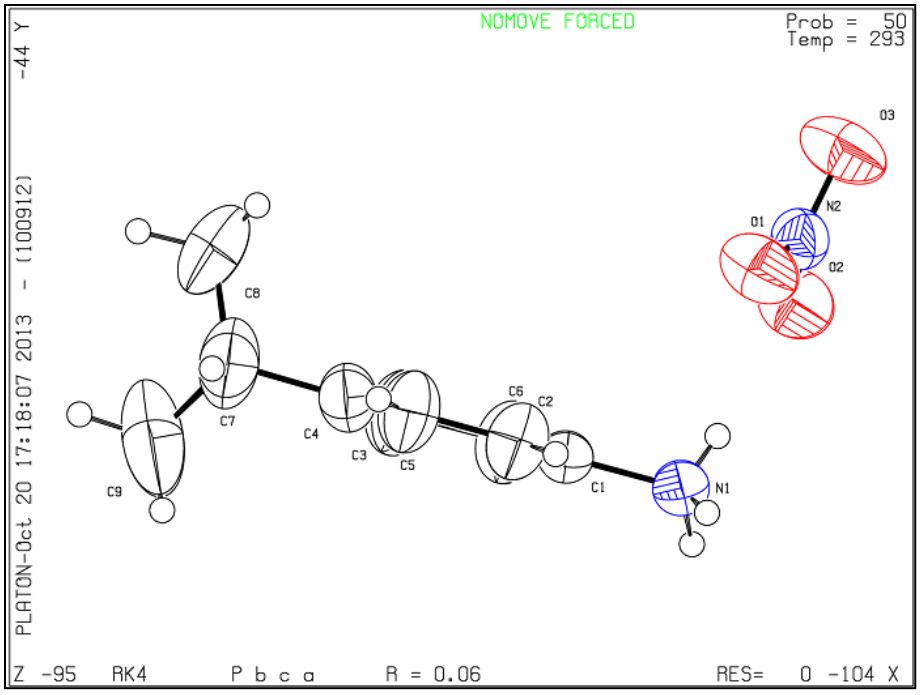

(e)

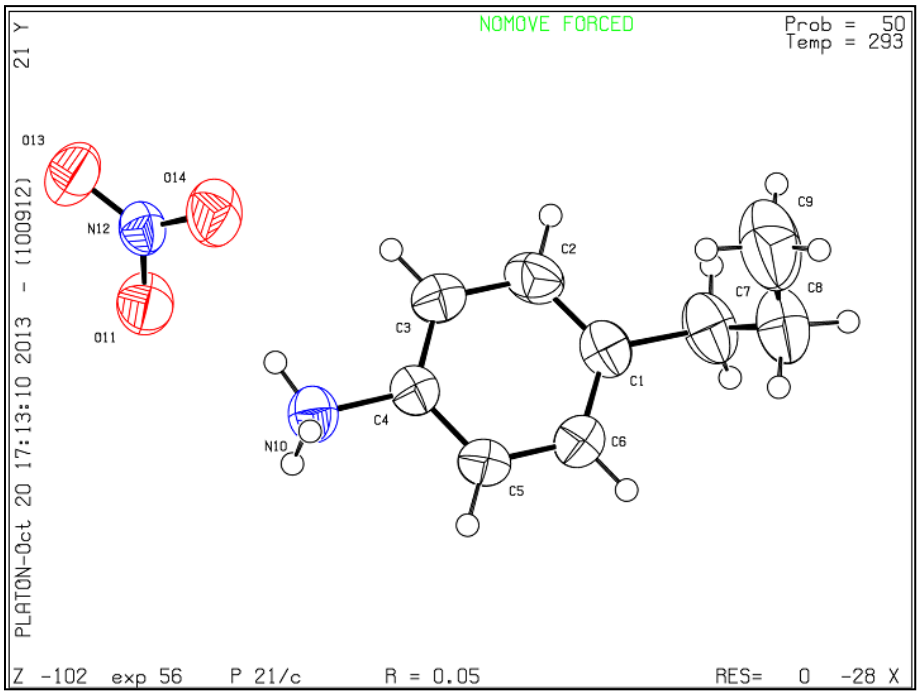

(f)

Fig. 3.10: Molecular view of compounds 4b (e) and 5 (f) having thermal ellipsoids are drawn at the 50% probability level

3.7.1:2 Gel Hair Crystals

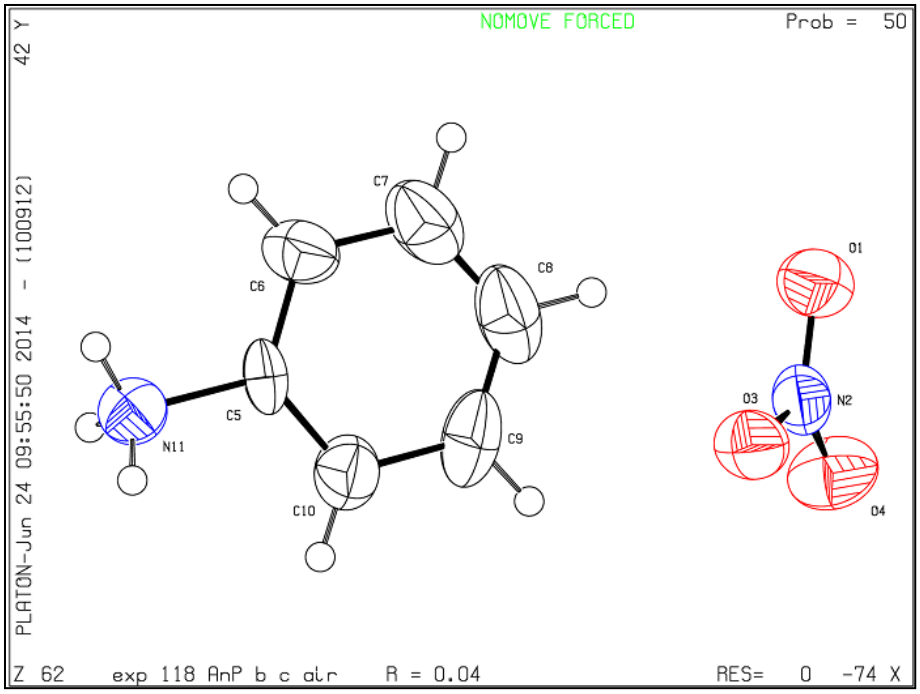

(a)

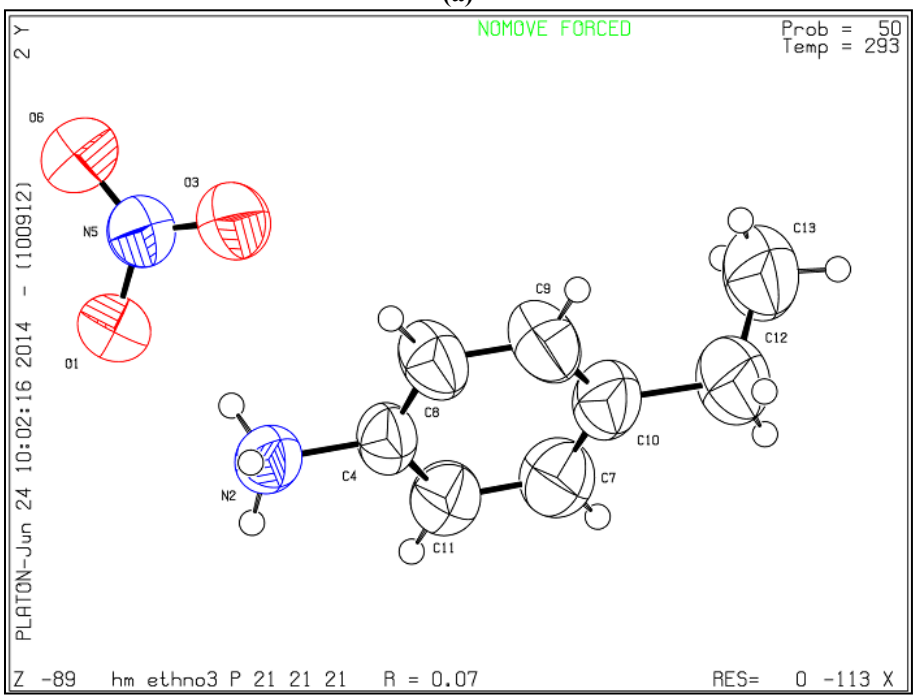

(b)

Fig. 3.11: Molecular view of compounds 1a (a) and 3a (b) having thermal ellipsoids are drawn at the 50% probability level

3.7.2 Designing

The single crystal study shows that ferroelectricity in KNO_3 [21] is observed in phase-III (γ-KNO_3, rhombohedral, space group *R3m* with a =5. 43Å and c = 9.112Å) at 295K. In crystal packing, K^+ and NO_3^- are alternately stacked along c-axis. Observed K—N distances along the c axis are 3.941Å and 5.051 A˚ (Figure 3.12a).

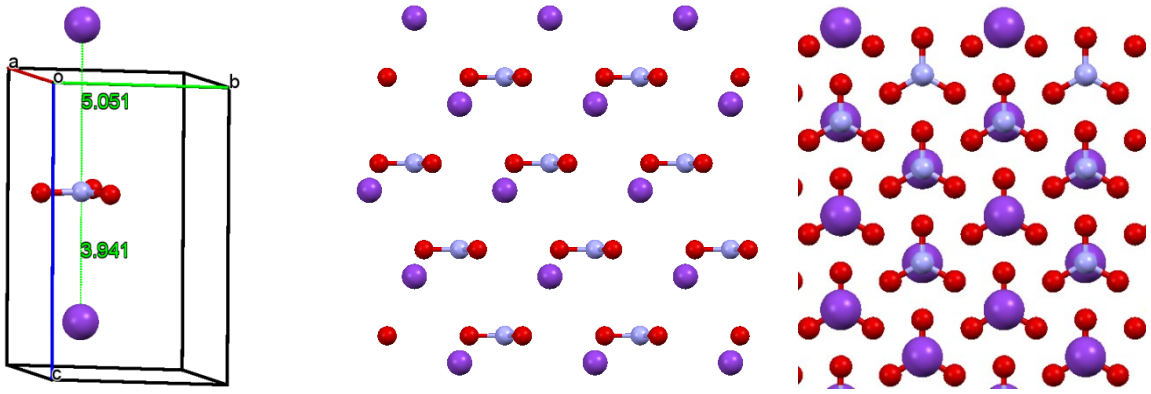

(a) (b) (c)

Fig. 3.12: Images of the KNO_3 crystal structure (a) variable K-N-K distances parallel along the *c*-axis (b) structure consists of alternating layers of K^+ and NO_3^- parallel along the *c*-axis and (c) viewed parallel to the *c*-axis

NO_3^- anion contains nonplanarity of around 0.011Å when distance measured from N atom to three oxygen plane. Elkabbany *et al*. [22] suggest from study of X-ray powder diffraction that ferroelectricity in KNO_3 is likely arises from the NO_3 group existing slightly off-center along the *c*-axis of the unit cell. Sawada *et al*. [23] found that reversal of the external electric field result into switching of NO_3^- between two K^+ i.e. change in K-N distance. This shift in the *c*-axis dimension is responsible for polarization and hence ferroelectricity.

Sugar like crystals of anilinium nitrate (**1b**) crystallizes in the orthorhombic system having space group *Pbca*, is reported in the literature [24]. The selected bond lengths and angles are listed in Table 3.9. Figure 3.13 depicts the crystal structure of $AnHNO_3$ (**1b**) along *c*-axis, here anilinium cation, AnH^+, is shown in a dot along with free perfectly planar nitrate anion. The structure shows nitrate and anilinium cation are equidistance (3.400 Å) from each other to form a chain, a case very similar to KNO_3 at room temperature.

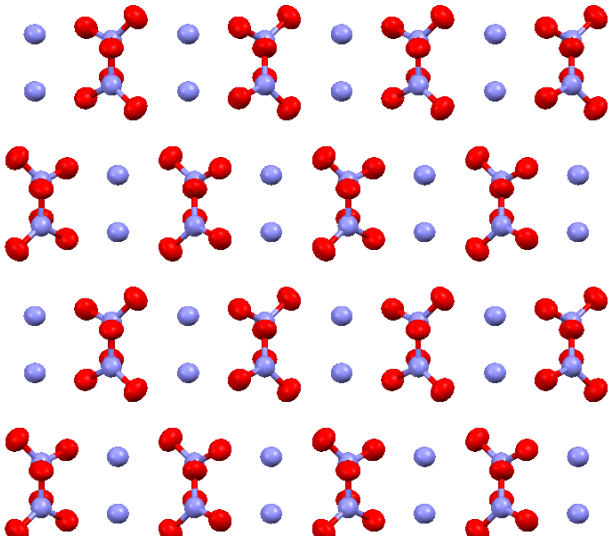

Fig. 3.13: Structure of AnHNO3 along *c*-axis, showing equidistant anilinium cation and nitrate anion, similar to KNO_3-phase-II

The anilinium cation is almost equidistance from three nitrate ions, similar to K^+. Additionally two important hydrogen bonding was observed in anilinium nitrate in the form of (i) hydrogen bonded (avg.2.850 Å) network with these nitrate anions are forming the layer of nitrate anions parallel to *ac*-plane. In the same plane nitrate anions are arranged opposite to each other while two anilinium cation lies at the center in between adjacent layers of nitrate anions. The phenyl moiety in the cation is arranged opposite to each other making an average angle of 71.03º for **1b** along the crystallographic *c*-axis. The angle between the single bonded nitrate nitrogen and nitrogen of anilinium cation (N^+-O-N^+) through oxygen is 104.30 Å. There are some short contacts at C2, C4 and C6 hydrogen's to the oxygen of nitrate anion making structure in a zigzag chain along the *b*-axis. (ii) It also formed continuous interwoven double helical like structure due to hydrogen bonding between nitrate and protonated anilinium cation along *c*-axis, as shown in Figure 3.14a.

There are six N–H---O hydrogen bonds (Figure 3.14b) with the length in the range of 2.82–3.20 Å with the average length equal to 3.01 Å. A very strong multi-component broad band with a maximum at approximately 2900 cm^{-1} represents the infrared absorption connected with it. One group of three bonds with similar lengths equal to 2.81, 2.86 and 2.88 Å gives the average value equals 2.85 Å. Three other hydrogen bonds with lengths 3.13, 3.17 and 3.20 Å constitute the second group with the average value of lengths equal to 3.17 Å.

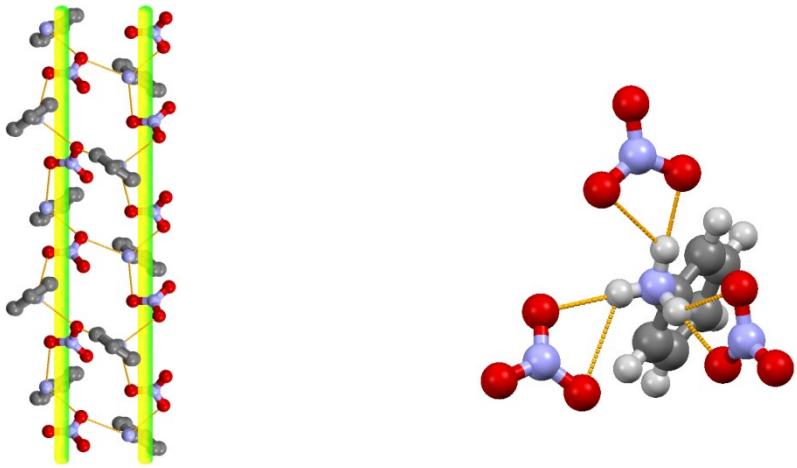

(a) **(b)**

Fig. 3.14: (a) Structure of $AnHNO_3$, showing interwoven double helical chains due to hydrogen bonding between anilinium cation and the nitrate anion along *c*-axis; (b) H-bonding pattern of $AnHNO_3$

Arrangement of interwoven double helical like structure in anilinium nitrate made us to think the introduction of substitute at 4- or *para*- position of phenyl moiety may result into structural change. Basically using steric factor one can change the angle of phenyl moiety and observe (a) change in position of anilinium cation/nitrate anion and/or (b) helical type pattern. Hence 4-toludine was employed initially to check validity of this hypothesis.

4-methyl anilinium nitrate (**2b**) crystallizes into $P2_1/n$ [25]. The asymmetric unit of **2b** contains a mono-protonated *p*-methylanilinium cation and nitrate anion link trough N-H···O hydrogen bond. Figure 3.15a depicts the crystal structure of 4-$MeAnHNO_3$ (**2b**) along *c*-axis. The selected bond lengths and angles are listed in Table 3.9. The structure shows nitrate and anilinium cation are not equidistance but it is 3.380Å and 3.454Å from each other to form a chain. These substitution at the para position leads changes in the position of *p*-methylanilinium cation, 4-$MeAnH^+$ and nitrate salt as compare to compound **1b**. Interestingly, interwoven double helical chains of **1b** get separated into **2b** as anti-parallel helical chains due to addition of substituent's of alkyl group at the para position (Figure 3.15b). This separation of helical chains has led us to the assumption that the particular substituent (4-ethyl) at the para position might give non-centrosymmetric structure depends on the observed H-bonding mode in **1b** and **2b**.

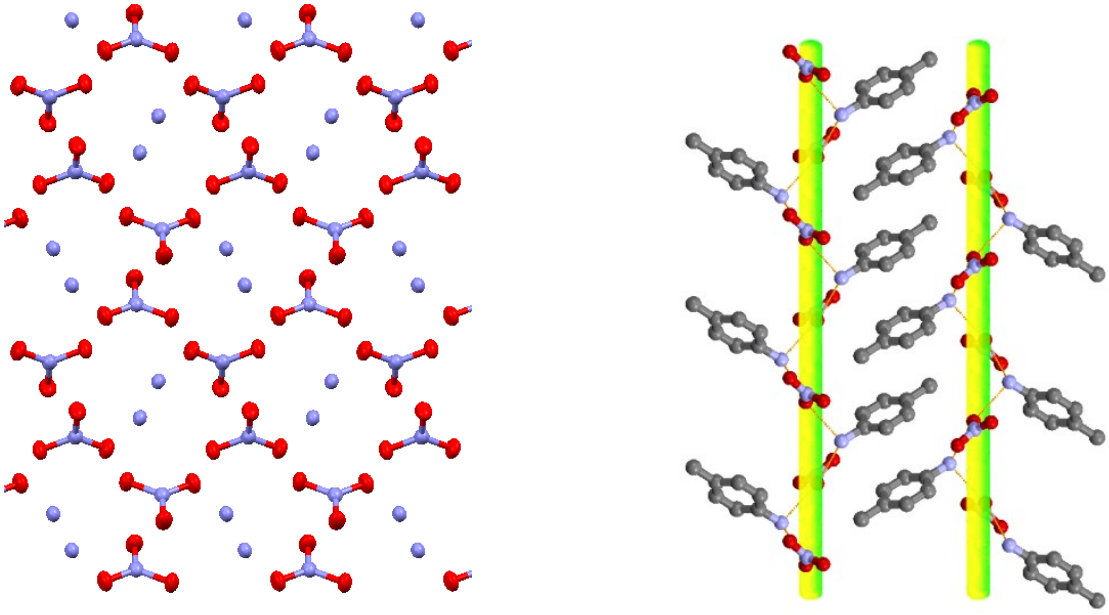

(a) (b)

Fig. 3.15: Structure of 4-MeAnHNO$_3$ along *c*-axis, showing non equidistant anilinium cation and nitrate anion in hexagonal arrangement of NO_3^- anions, similar to KNO$_3$-phase-II: (b) Hydrogen bonding assisted anti-parallel helical chains

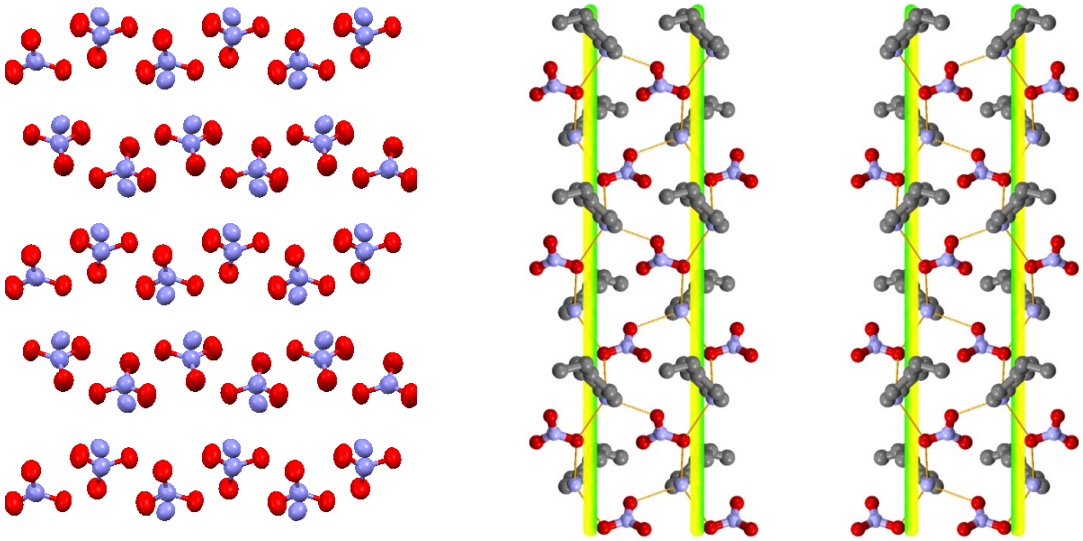

(a) (b) (c)

Fig. 3.16: (a) Hexagonal arrangement of NO_3^- anions showing *p*-eAnH$^+$ above/below the plane for 3a/3b; Hydrogen bonding assisted (b) left handed (*M*) helical chains : (c)) right handed (*P*) helical chains

Hence we synthesized 4-ethyl anilinium nitrate (**3b**) and studied its crystal structure. As per expectation, 4-ethyl anilinium nitrate (**3b**) crystallizes into chiral space $P2_12_12_1$ and formed one dimensional homochiral helical chain forming the conglomerates (**3b-*P*** and

3b-*M*) due to intermolecular hydrogen bonding between anilinium cation and the nitrate anion. The selected bond lengths and angles are listed in Table 3.9.

Interesting fact is that the small difference change in *para*-substitution from methyl (**2b**) to ethyl (**3b**) group leads to a substantial difference in space group with the spontaneous chiral resolution of enantiomeric forms of helices. The homochiral helical chains resolved into separate crystals as right handed as well as left handed helical chain isomers. Due to formation of helical chain the structure crystallizes into non-centrosymmetric system.

To check that another substituent might give polar as well chiral space group, we have introduced 4-isoproyl and 4-*n*-propyl group on aniline and synthesized there nitrate salts.

4-isopropyl anilinium nitrate (**4b**) crystallized into *Pbca* space group while 4-propyl anilinium nitrate (**5b**) crystallizes into *P21/c* space group. Compound **4b** formed the interwoven hydrogen bonding assisted double helical chains same as **1b** while in **5b** the helical chains get separated and formed opposite direction helical chains. The average H-bond lengths are **4b**-2.895Å and **5b**-2.871Å. Here nitrate ion and anilinium cations are not in one plane, anilinium cation lies above the plane of nitrate anion. Anilinium cation is not equidistance from three nitrate ions, the distances being 3.625, 3.387, 3.522 in case of **4b** while 3.442, 3.487, 3.659 in case of **5b**.

Hence arrangement in **4b** and **5b** proves that the introduction of substitute at 4- or *para*-position of phenyl moiety result into structural change and one can design and synthesized compounds in chiral/polar state to obtain desired property.

3.7.3 Structure Evaluation for chirality

Figure 3.17 (1b-3b) shows the change in position of nitrate anion and anilinium cation (black circle) with increasing substituent's at para position. To understand this change we compare all three crystal structures with each other.

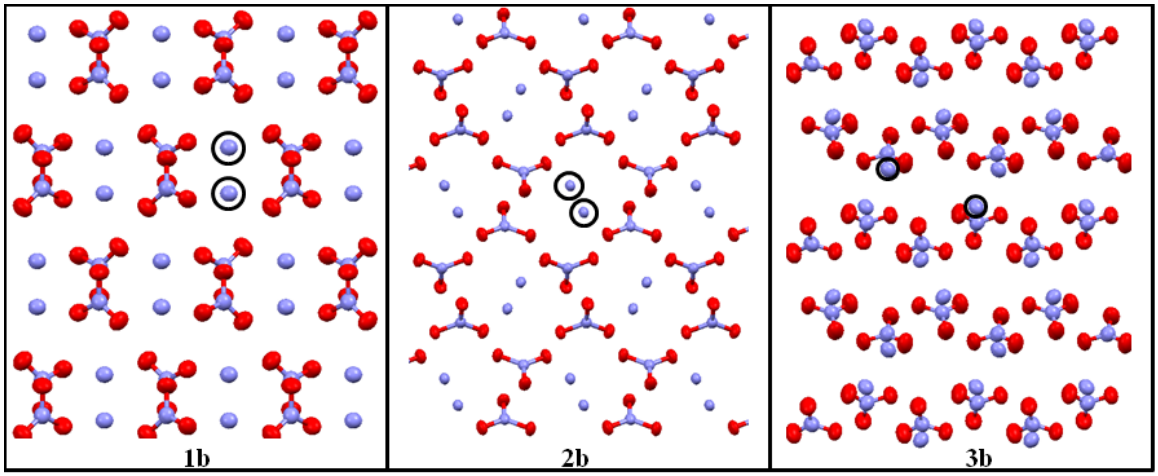

Fig. 3.17: Packing of the crystal structure of along the *c*-axis; carbon and hydrogen atoms are omitted for clarity

In **1b**, the anilinium cation and nitrate are equidistant from each other and forming hexagon like structure along *c*-axis (Figure 3.17-1b). The opposite phenyl moiety in the cation (AnH^+) making an angle of 70.13 Å. In **2b**, *p*-$mAnH^+$ cations and nitrate are not equidistant from each other and arranged the same way as in **1b,** surrounded by six nitrate molecules making hexagonal layer formation which are opposite to each other and the *p*-$mAnH^+$ cation sits between these hexagons, shown in Figure 3.17-2b. Contrary to **1b** adjacent 4-me phenyl moiety is found parallel to each other in crystal packing. The ethyl group in **3b** is not in the plane with the phenyl ring and has an angle of 65.06 Å. Here also crystal packing forms a hexagonal structure of nitrate anion but *p*-$eAnH^+$ cation lie above and below the nitrate anion which distinguishes it from **1b** and **2b** in which the cation always present at central position of hexagon like structure. Adjacent *p*-$eAnH^+$ moiety is not mutually perpendicular to each other as observed in **1b**, making an angle of 83.19 Å.

Similar to **1b**, an anilinium cation in **2b** and **3b** is hydrogen bonded to three different nitrate anions. The average hydrogen bond lengths are **2b-** 2.854Å and **3b**-2.889 Å. Nitrate

ion and anilinium cations are not in one plane, anilinium cation lies above the plane of nitrate anion. In **2b** and **3b** an anilinium cation is not equidistance from three nitrate ions, the distances being 3.380, 3.454, 3.490 Å in case of **2b** and 3.432, 3.470, 3.554 in case of **3b**. In the same layer of nitrates, nitrate planes (along *a*-axis) lay one above and parallel with a distance of 1.130 Å (**2b**) and 0.713 Å (**3b**). The neighboring nitrate layers make an angle to each other.

Bond length of single hydrogen bonded O (NO_3) distance (1.241-**1b**, 1.255-**2b**, 1.264-**3b**) as well as angle (104.30º-**1b**, 111.94º-**2b**, 114.55º-**3b**) is increasing from **1b** to **3b** resulting the structure of **3b** force to crystallize into chiral state and results into separation of helical chains into separate homochiral crystals. The *para*-position substituent group increased the distance and angle changed substantially causing helicity in structure is induced and hence chirality. e.g. **1b** having a double helical type H- bonding while **2b** having alternative helical type H-bonding, but in opposite direction cancel the chirality of induced chirality. In **3b**, this distance increased which results in hydrogen bonding assisted helicity and crystallization into the chiral space group.

There is small non planarity in NO_3 anion from oxygen plane in **3b** as compared to **1b** and **2b** nitrate anion. The nitrogen lies above the three oxygen plane, creating non planarity having a distance of 0.009Å.

The anilinium cations in **2b** and **3b** seems to be come in between the layers of nitrate anion and closer to the one of the layer along *b*-axis, hence the chances of originating Chirality increases. In **2b** the helical pitch slightly shifted from one another, but the adjacent helical pitch lie opposite in direction which makes the helicity cancel by each other making it crystallized into the non chiral space group. While in **3b** the helical pitch shifted more compared to **2b** due addition of methyl group (4-ethyl) causes the adjacent helical chain to adopt the same direction. Hence, chirality developed through helicity of chain which remain in the same direction. The CD spectra support the coexistence of left-handed and right-handed enantiomers in one pot, which confirms spontaneous resolution occurred during the course of the crystallization and confirm the chirality and helicity relation. The bulk sample showed a silent CD spectrum. Hence all results confirmed that the resulting crystals of **3** are racemic mixture.

3.7.4 Gel Hair Crystals

Ionic bonding driven unusual crystal growth of tubular organic nitrate salts using a simple gel-mediated method which generates different morphologies ($AnHNO_3$-**1a**) was reported previously by our group [24b]. KNO_3 and $NaNO_3$ are inorganic analogues of these organic salts, and have shown ferroelectric behavior at high temperature. Nitrate salts of $AnHNO_3$-**1a** and 4-Et$AnHNO_3$-**3a** showed ferroelectricity at room temperature.

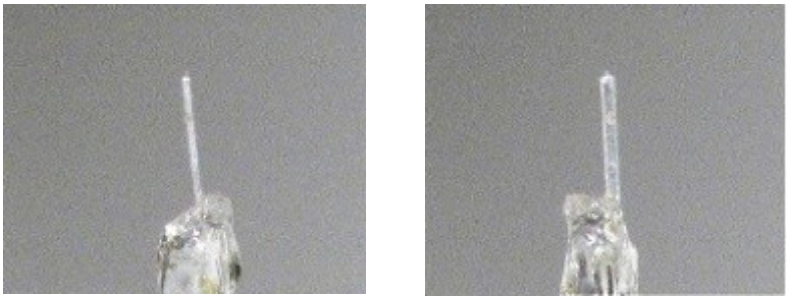

1a **3a**

Fig. 3.18: Pictures of hair like crystals of compound 1a and 3a

We repetitively attempted crystal structure of these hairs like crystals of **1a**. After many attempts we succeeded in solving the crystal structure of hair like crystals of anilinium nitrate salt (Figure 3.18). $AnHNO_3$-**1a** also crystallizes in *Pbca* (orthorhombic) space group, Z = 8 and showed similar crystal packing as that of sugar like crystals (**1b**) at room temperature.

We also synthesized 4-ethyl anilinium nitrate hair like crystals and study its crystal structure. It showed similar crystal packing (orthorhombic, $P2_12_12_1$) as that of needle like crystal structure of **3b**.

Anilinium cation in **1a** and **3a** is hydrogen bonded to three different nitrate anions contain average hydrogen bond length are **1a-** 2.850Å and **3a**-2.904 Å respectively. Anilinium cation in **1a** and **3a** are not equidistance from three nitrate ions contain 3.396, 3.424, 3.434 Å in case of **1a** and 3.411, 3.420, 3.524 Å in case of **3a**. The phenyl moiety in the cation is arranged opposite to each other making an average angle of 70.13 Å for **1a** and 71.03 for **3a** along the crystallographic *c*-axis.

In gel hairs crystals of **3a** structure crystallized into chiral state and formation of

homochiral crystal. Nitrogen atom found to be lays above the three oxygen plane in **1a** (0.030Å) and **3a** (0.046Å) creating non planarity in NO_3^- anion.

Overall one can consider that both crystal structures of **1a** and **1b**; **3a** and **3b** are similar. Though the gel hair crystals giving ferroelectricity in non polar and centrosymmetric system-*Pbca* of **1a** and in non polar and non-centrosymmetric system- $P2_12_12_1$ of **3a**.

3.7.5 Structure-Property relations

Compound **1b** and **2b** crystallizes into non chiral/non polar (centrosymmetric) space group while **3b** crystallized in non-centrosymmetric system (chiral) which is not one of 88 ferroelectric but is one of the 94 ferroelastic space group [26]. But all these crystals i.e. **1b-3b** does not showed any ferroelectricity at RT.

On the contrary, hair like crystals **1a** and **3a** showed room temperature ferroelectricity/ ferroelasticity though they crystallized into similar space group as that of **1b** (*Pbca*) and **3b** ($P2_12_12_1$) respectively. We also search possibility of *pseudo*-symmetry might be involved in **1a** and **3a**. *Pbca* (61) space group involves subgroups includes $Pca2_1$ (No. 29), $P2_12_12_1$ (No. 19), and $P2_1/c$ (No. 14) while $P2_12_12_1$ (No. 19) space group involves subgroups includes $P2_1$ (No. 4), $P2_1/c$ (No. 14) and $P2_1$ /m (No. 11). Hence data reduction followed by data refinement gives higher *R* indexes value in these subgroups minimizing possibility of *pseudo*-symmetry.

Hence we studied both crystal (**1a/1b** and **3a/3b**) structures carefully to detect the reason behind the ferroelectricity. In structure comparison we observed change in (i) arrangement of phenyl ring; (ii) N^+-O^----N^+ hydrogen bond and (iii) angle between diagonally arranged NO_3^- anion.

3.7.5.1 Structure comparison of 1a and 1b

The phenyl moiety in the anilinium cation is arranged opposite to each other making an average angle of 71.36 Å for **1a** and 71.09 Å for **1b** along the crystallographic *c*-axis. Hence difference in angle by 0.3 Å. In **1a** and **1b**, anilinium cation molecules are placed into channels running parallel to the *c*-axis across the crystal. The anilinium molecules in **1a** and **1b** are elongated almost perpendicularly to the polar binary *a*-axis, which gives

rise to an anti-parallel arrangement of the push–pull fragments. In **1a**, angle change between these anti parallel anilinium cation was observed by 0.3 Å compared to **1b** due to which it moved slightly away from polar binary *a*-axis. This small angle change movement induces polarity in crystal structure.

$$\text{mmm } (D_{2h}) \xrightarrow{\text{mmm}F\text{mm2}} \text{mm2 } (C_{2v})$$

Scheme 3.5: uniaxial ferroelectric phase transitions with Aizu notations

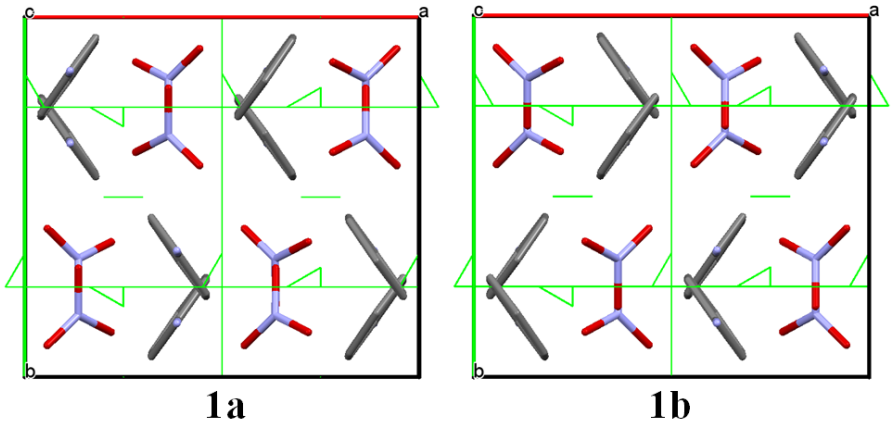

1a **1b**

Fig. 3.19: Packing and symmetry element 2_1 screw axes of the crystal structure of 1a and 1b along the *c*-axis

Figure 3.19 shows the symmetry element 2_1 screw axes along *c*-axis. It is clear that due to change in angle in **1a**, changes the Aizu notation as shown in Scheme 3.5, where *F* means ferroelectric phase.

It is further supported by variable temperature FT-IR spectra. Variable temperature FT-IR spectra confirmed that lowering of symmetry of the NO_3^- ion from D_{3h} to C_{2v} or *Cs* (Scheme-3.5). Hence From a microscopic change can alter the electric property associated with it.

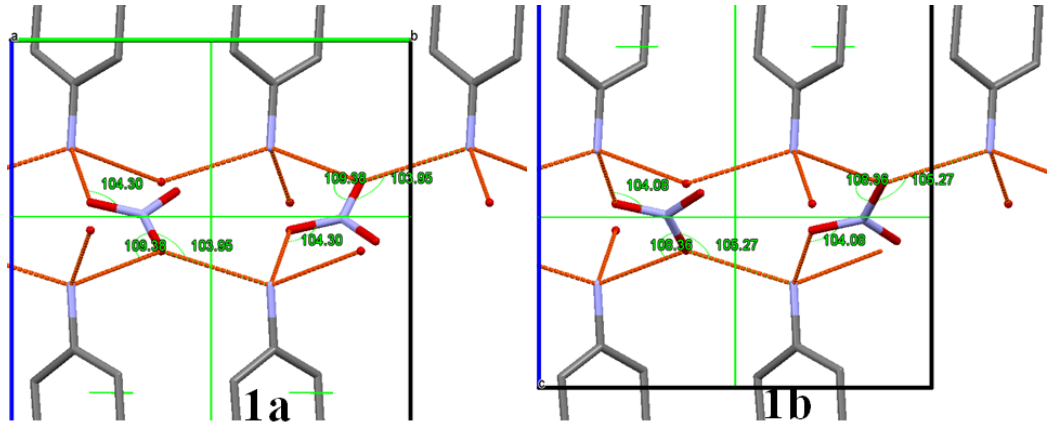

Fig. 3.20: Hydrogen bond angles between N^+-O^----N^+ along a-axis in 1a and 1b

Phenyl ring displacement changes hydrogen bond angles between NO_3^- and ammonium cation (Figure 3.20). The hydrogen bond angles between N^+-O^----N^+ in **1b** are 103.95º, 104.30º and 109.38º. These angles changes on displacement of phenyl ring by 1-2º in **1a**. The angles in **1a** become 104.08º, 105.27º and 108.36º. This small displacement lowers down symmetry of the NO_3^- ion from D_{3h} to C_{2v} and creates polarity along *a*-axis in crystal structure of **1a** result into ferroelectricity.

Furthermore, the results of differential scanning calorimetry (DSC), an endothermic peak are clearly observed at 117.03 ºC and 109.76 ºC corresponding to the ferro-to-ferroelectric in **1a** and para-to-ferroelectric transition in **1b**. The values of ΔH are estimated as -40.16 Jg^{-1} and -46.71 Jg^{-1} while ΔS values 49.56 Jg^{-1} and 46.89 Jg^{-1} for **1a** and **1b** respectively. Hence energy involved in the endothermic transition is much less than the energy released during the exothermic transition and displays a long tail on the lower temperature side of the thermal anomaly which suggests the disorder–order feature (second-order) phase transition. We failed to obtained high temperature crystal structure data due to loss of crystallinity.

3.7.5.1 Structure comparison of 3a and 3b

To explain the ferroelectric character of **3a** we compare it to KNO_3 (ferroelectric stage) crystal structure. The crystal structure of **3a/3b** shows that the both cations are not completely stacked as the structure of ferroelectric phase KNO_3 but it is slightly away from the nitrate ion (Figure 3.21b). It is giving similar arrangement of KNO_3 crystal type arrangement, only difference is that the alternative direction of nitrate and anilinium cation is observed.

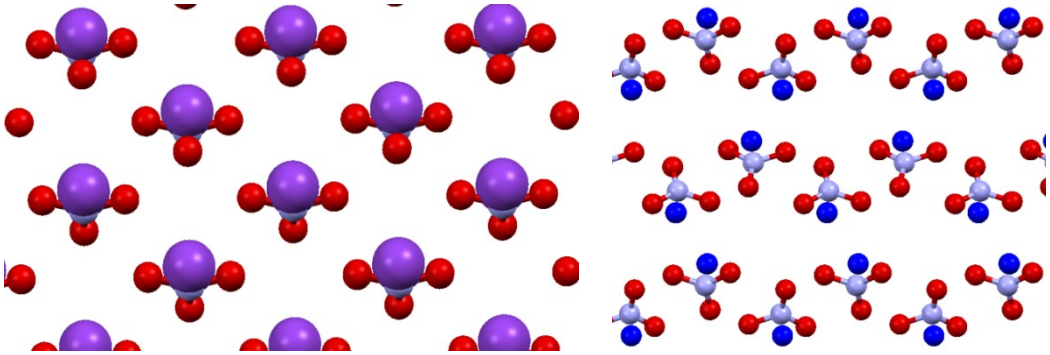

(a) (b)

Fig. 3.21: Arrangement of cation and anion (a) KNO_3 and (b) 3b

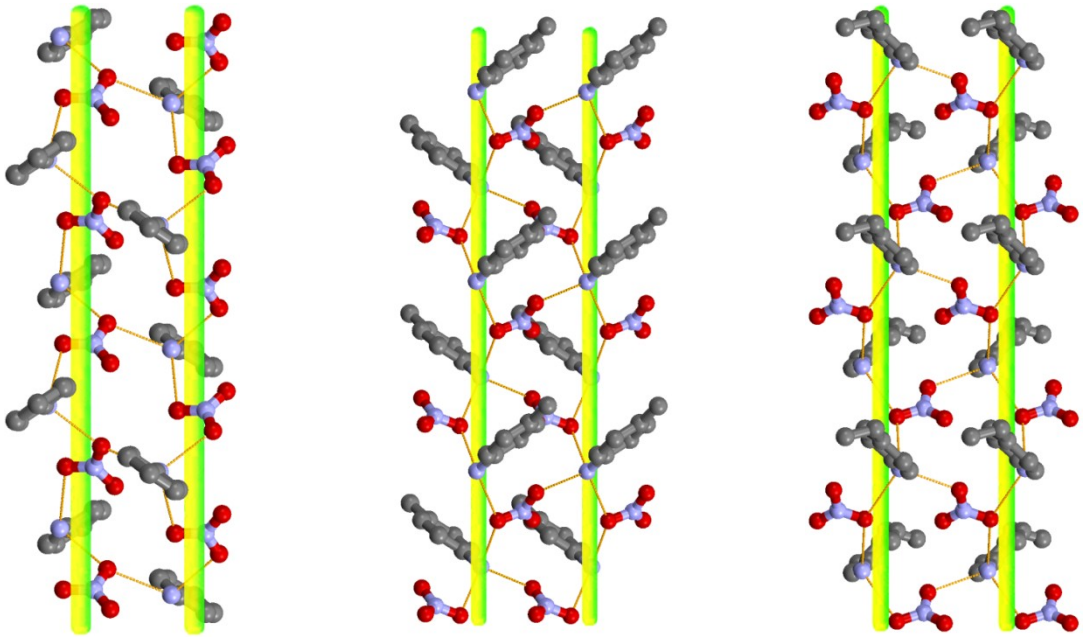

(a) (b) (c)

Fig. 3.22: Hydrogen bonded assisted helical chains between anilinium cation and the nitrate anion along *c*-axis (a) 1b; (b) 2b and (c) 3b

The **1b** has anilinium cation in plane with nitrate anion and it cancels the polarization in the layer itself as they run in the opposite direction (Figure 3.22a). **2b** having polarization as the anilinium cation not in the plane of nitrate anion but as the helical structure is completely super imposable on each other hence the polarization cancels out decreasing the chances of ferroelectricity (Figure 3.22b). In **3b** the helical chains are not super imposable on each other hence the ferroelectricity is present at room temperature (Figure 3.22c).

In KNO_3, the ferroelectric ordering is predicted on the basis of rotations of hexagonally packed nitrate anion in a systematic manner to induce polarization. We expect similar mechanism for ferroelectric behavior in 4-ethyl anilinium nitrate salt (**3a**). But, apart from this what we observed is the change in planarity of the NO_3^- ligand when an ethyl group in introducing at the para position in $AnHNO_3$. Now, if one considers the more electronegativity of *p*-eAnH+ over AnH+, then H^+ is attracted to the earlier base more effectively. Is this motion of H^+, to get attracted to Lewis base, is inducing change in NO_3^- rotation and hence the ferroelectric behavior? If the answer is yes, then it is closely related to KDP type ferroelectric behavior. One needs to closely study the 'driving force' for ferroelectric behavior in this system more carefully to reveal answer. Thus, a simple synthetic strategy and effective use of polymorphism can be extended to other class of ferroelectrics to explore 'Molecular Ferroelectrics' for various applications.

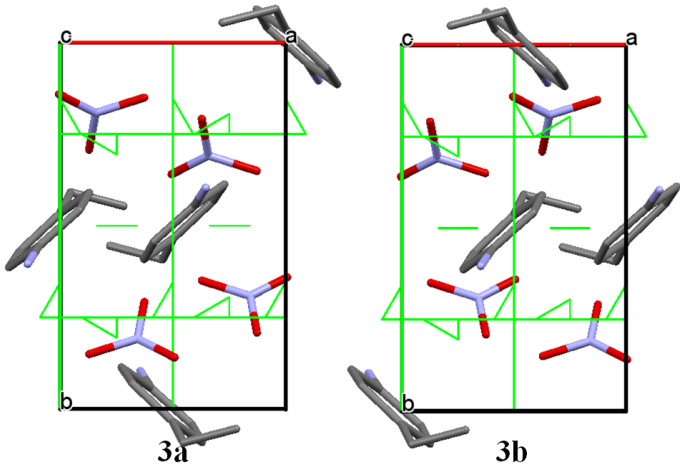

Fig. 3.23: Packing of the crystal structure of 3a and 3b along the *c*-axis

Here also, we studied and compared both **3a** and **3b** crystal structures carefully to detect the reason behind the ferroelectricity in **3a** and not in **3b**. The projection of the unit-cell showing the symmetry element 2_1 screw axes along *c*-axis is shown in Figure 3.23.

The phenyl moiety of the cation is arranged opposite to each other making an average angle of 82.72 Å for **3a** and 83.63 Å for **3b** along the crystallographic *c*-axis. The hydrogen bond angles between N^+-O^----N^+ in **3b** are 96.73º, 102.00º, 106.93º and 113.94º. These angles changes on displacement of phenyl ring by 1-2º in **3a**. The angles in **3a** become 97.32º, 102.13º, 106.92º and 113.21º.

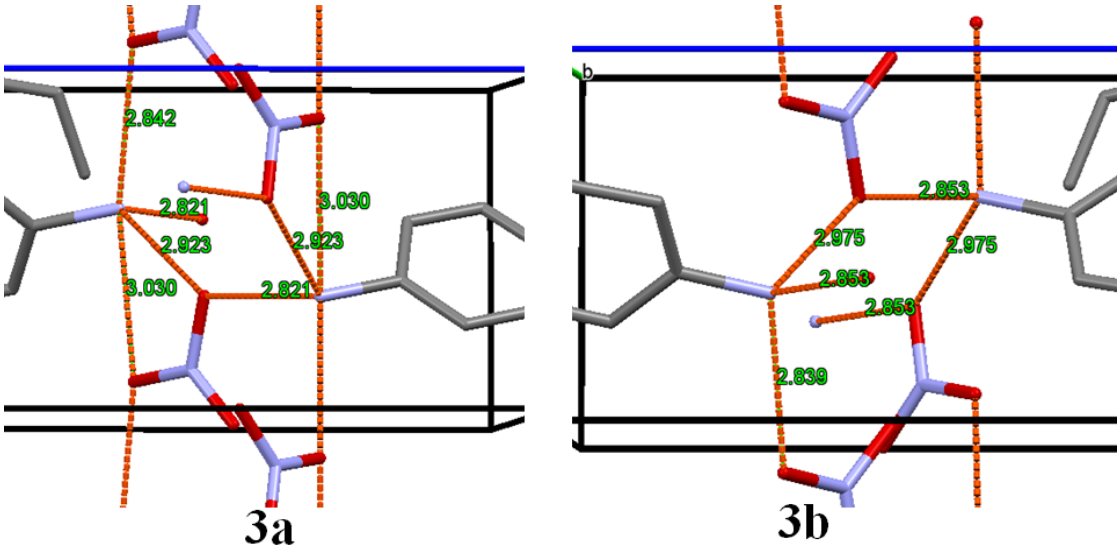

Fig. 3.24: Hydrogen bond angles between N^+-O^----N^+ along a-axis in 3a and 3b

One *p*-eAnH^+ molecule of **3a** lies on the binary axis along *a*-axis, while in **3b** it lies at centre of the axis. The angle between two diagonally arranged nitrate anions are also varied in **3a** (88.20º) and **3b** (88.64º) along *a*-axis. This small displacement of phenyl ring and nitrate anion creates microscopic polarity in **3a** along *b*-axis.

DSC measurements on **3a**/**3b** confirm that observed transition is of second-order. Upon heating and cooling, the crystalline sample of **3a** and **3b** undergoes a single phase transition at ca. 76.35 ºC and 74.70 ºC, showing an exothermic peak at 41.72 ºC in case of **3b** only. The two observed peaks demonstrate a reversible phase transition with a large heat hysteresis. Both the thermal hysteresis and the shape of the peaks testify the character of

a second-order phase transition, in good agreement with that found in variable-temperature Single Crystal X-ray diffraction.

We study variable temperature X-ray single crystal diffraction on **3b** only as it showed reversible phase transition. Variable temperature X-ray single crystal diffraction on **3a** is impossible to perform due to its crystal size. Similar phase transition was observed in case of **3a**, hence as a representative variable temperature X-ray single crystal diffraction data of **3b** can be considered for **3a**.

Table 3.8: Crystal structure and refinement parameters for 3b-HT

Identification code	**3b-HT**
Empirical formula	$C_8H_9N_2O_3$
Formula weight	181.17
Temperature/K	353.00(10)
Crystal system	Orthorhombic
Space group	Pbca
a/Å	9.4724(15)
b/Å	10.5203(14)
c/Å	20.297(2)
α/°	90.00
β/°	90.00
γ/°	90.00
Volume/Å^3	2022.7(5)
Z	8
ρ_{calc}g/cm^3	1.190
μ/mm^{-1}	0.784
F(000)	760.0
Crystal size/mm^3	0.29 × 0.21 × 0.2
Radiation	CuKα (λ = 1.54184)
Reflections collected	4486
Independent reflections	1990 [R_{int} = 0.0248, R_{sigma} = 0.0303]

Data/restraints/parameters	1990/0/218
Goodness-of-fit on F^2	1.178
Final R indexes [I>=2σ (I)]	$R_1 = 0.0836$, $wR_2 = 0.2068$
Final R indexes [all data]	$R_1 = 0.1521$, $wR_2 = 0.2577$
Largest diff. peak/hole / e Å^{-3}	0.13/-0.13

At phase transition (solid-solid) temperature, compound **3b** crystallized into centrosymmetric space group *Pbca* without any polarity in the structure confirmed by the disordered crystal structure as shown in Figure 3.25 a-d.

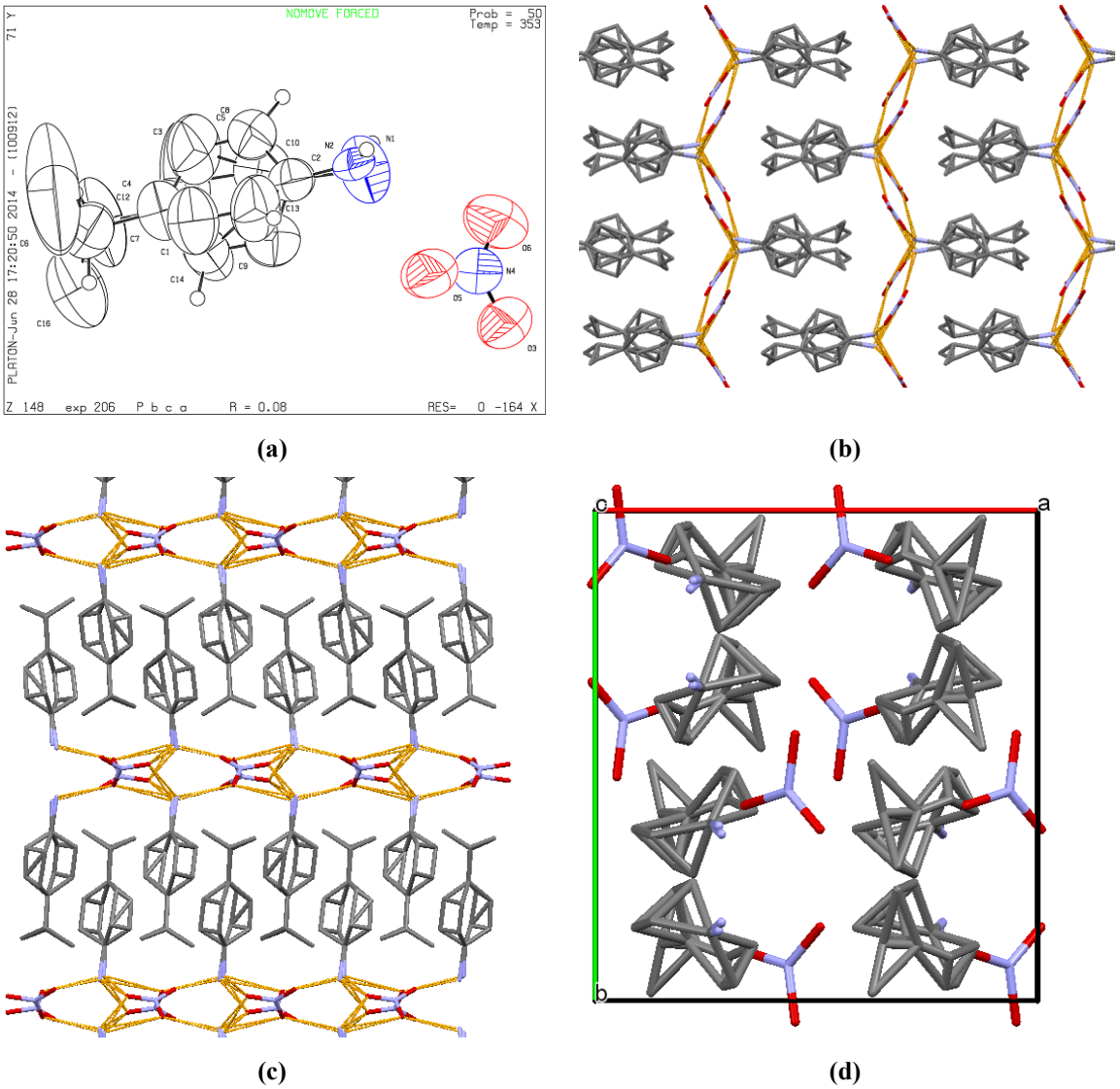

Fig. 3.25: (a) Molecular view of compounds 3b-HT having thermal ellipsoids are drawn at the 50% probability level; (b) Structure of 3b-HT along *b*-axis showing similar hydrogen bonded assisted helical chains as 1b; (c) Structure of 3b-HT along *a*-axis; (d) Structure of 3b-HT along *c*-axis

The molecular mechanism of the paraelectric–ferroelectric transition is found to be due to a motion of the organic cations ($4eAnH^+$). In paraelectric phase, eight crystallographically related $4eAnH^+$ cations (placed in the special positions) are disordered and do not contribute to the ferroelastic properties. Tilted 4eAnH+ cation in **3b** became straight as that of anH^+ in **1b** results into rearrangement of hydrogen bonding and change in position of nitrate anions. Two nitrate anions came closer with rotation of around 20º around *c*-axis. In the ferroelectric phase these cations became ordered, continuously with temperature, being fully ordered at temperatures at which one can observe saturated spontaneous polarization.

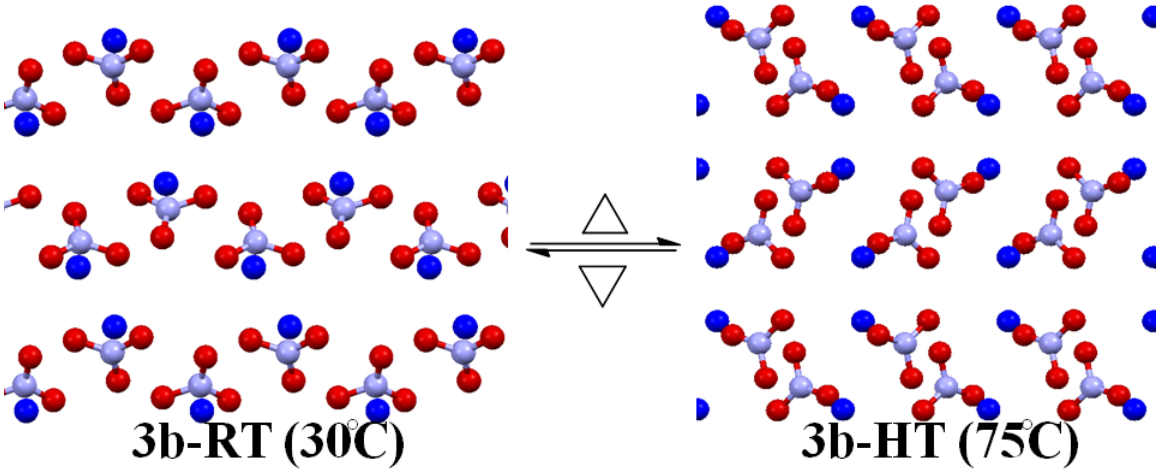

Fig. 3.26: Reversible phase transition of 3b-RT ($P2_12_12_1$) to 3b-HT (*Pbca*) showing change in rearrangement of cation and nitrate anion along *c*-axis

This transition is believed to ferroelastic in nature. High temperature phase has *Pbca* symmetry while room temperature phase has symmetry $P2_12_12_1$ [27]. The ferroelastic phase space group $P2_12_12_1$ (19) should be a subgroup of the paraelectric phase *Pbca* (61) whose subgroups includes $Pca2_1$ (No. 29), $P2_12_12_1$ (No. 19), and $P2_1/c$ (No. 14) obeying the Curie symmetry principle [28] and suggesting that this phase transition should be second-order. Also, spatial symmetry operations, increase from 4 to 8 (Scheme 3.6), being in good agreement with the macroscopic symmetry element analysis.

A centrosymmetric crystal structure formed the double helical type networked same as of **1b** which showed a centrosymmetric space group *Pbca* while on cooling compound **3b** undergoes *Pbca*-$P2_12_12_1$ ferroelastic phase transition from centrosymmetric orthorhom-

bic high-temperature phase to a noncentrosymmetric orthorhombic room-temperature phase at 42ºC.

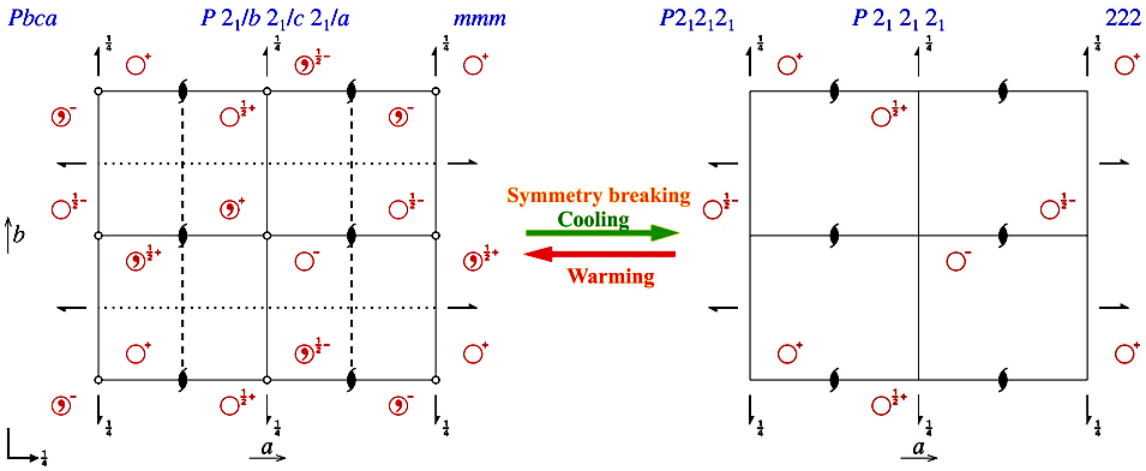

Scheme 3.6: Spatial symmetry operations changing from paraelectric phase (*Pbca*) to ferroelectric phase ($P2_12_12_1$) in 3b

The changes in the hydrogen bonding pattern on decreasing temperature may be a decisive parameter leading to the ordering of the cations below 42 ºC and the formation of a chiral space group of $P2_12_12_1$ where the symmetry elements halve from 8 (E, C_2, $2C_2$' i, $3\sigma_h$) to 4 (E, C_2, $2C_2$') confirms the second order transition (Landau phase transition theory). Rapid decrease in the volume of the crystal of about 48.10% is clearly observed. From a microscopic point of view, the loss of n-glide mirror results in the loss of inversion center *i*. The two-fold C_2 remains unchanged, leading to the final low-temperature space group of $P2_12_12_1$.

Because the paraelectric ferroelectric phase transition is a structural phase transition, a detailed structure analysis is indispensable for understanding of the origin of ferroelectricity/ ferroelasticity, which may be the displacement of ions or the order-disorder transitions of electrically active groups in the crystal lattice. However, structural analysis of the paraelectric and ferroelectric phases of a crystal compound is often difficult because small displacements of the ions are highly correlated with each other and with thermal parameters, which can result in inaccurate refined values and multiple solutions.

In a ferroelastic structure, several ferroelastic domain states can be formed [29]. These states have the same crystal structure and differ only in the orientation with respect to the coordinate system of the paraelastic phase. Since all domain states are energetically equivalent, they can coexist in the same crystal. In order to confirm the ferroelastic property in the crystal, the domain structures were observed by employing optical polarizing microscope [30]. The domain patterns at room temperature (RT) and at high temperature (HT) are shown in Figure 3.27.

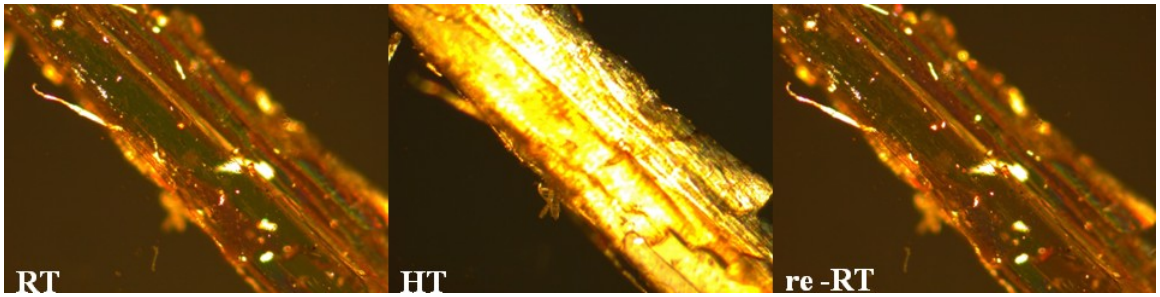

(a)

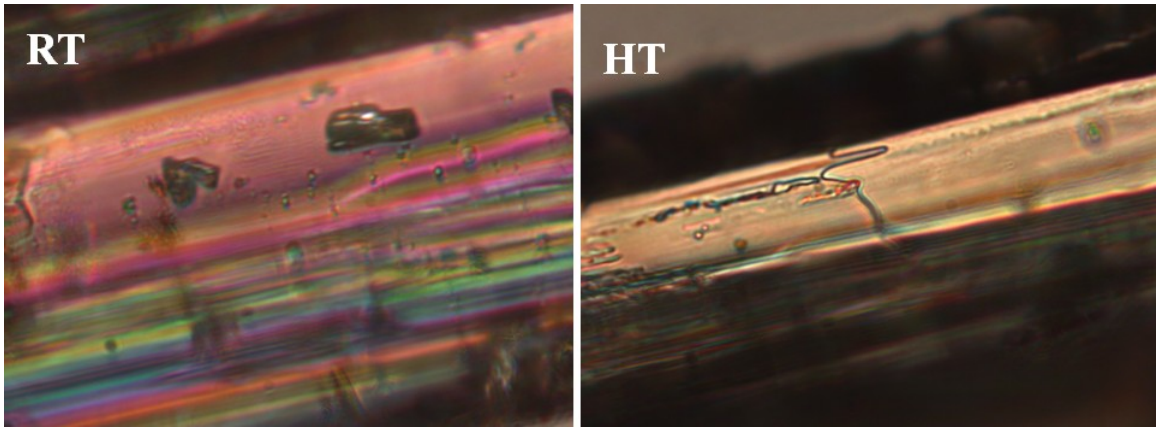

(b)

Fig. 3.27: Domains walls as function of temperature (30-75 ºC) by polarizing microscope. The sample was placed between two polarizers that make an angle (a) 0° (re-RT sample after cooling down to the initial stage) and (b) 45°

The optical observations of the sample under a polarizing microscope at the room temperature phase showed that the crystal under investigations exhibits a ferroelastic domain structure. In the high temperature phase, domain pattern get decreased and in some area totally diminished. Hence high temperature phase appear as paraelastic phase. Taking

into account all the above mentioned facts we suggest that the RT→HT phase transition is of the ferroelastic–paraelastic type.

Table 3.9: Selected bond lengths (Å) for compounds 1a, 1b, 2b, 3a, 3b-M and 3b-P

	1a	1b	2b	3a	3b-M	3b-P
N1—O1	1.235 (4)	1.2669 (9)	1.271 (2)	1.265 (5)	1.252 (2)	1.212 (4)
N1—O2	1.234 (4)	1.2414 (9)	1.255 (2)	1.246 (6)	1.246 (2)	1.264 (3)
N1—O3	1.274 (4)	1.2294 (9)	1.227 (2)	1.207 (6)	1.210 (2)	1.262 (4)
N0—C1	1.476 (5)	1.4662 (10)	1.468 (3)	1.478 (6)	1.465 (2)	1.474 (4)
C1—C2	1.361 (6)	1.3723 (12)	1.384 (3)	1.348 (7)	1.369 (3)	1.375 (4)
C1—C6	1.364 (6)	1.3748 (12)	1.375 (3)	1.359 (7)	1.371 (3)	1.368 (5)
C2—C3	1.378 (6)	1.3870 (13)	1.380 (3)	1.384 (7)	1.382 (3)	1.375 (5)
C3—C4	1.354 (7)	1.3666 (16)	1.392 (3)	1.384 (8)	1.378 (4)	1.376 (6)
C4—C5	1.361 (6)	1.3675 (16)	1.391 (3)	1.372 (9)	1.385 (4)	1.391 (6)
C5—C6	1.391 (6)	1.3900 (14)	1.384 (3)	1.394 (8)	1.383 (3)	1.391 (5)
C4—C7			1.499 (4)	1.565 (8)	1.526 (3)	1.550 (5)
C7—C8				1.430 (9)	1.473 (5)	1.474 (8)

Table 3.10: Selected bond angles (º) for compounds 1a, 1b, 2b, 3a, 3b-M and 3b-P

	1a	1b	2b	3a	3b-M	3b-P
O2—N1—O1	117.9 (5)	118.46 (6)	117.28 (19)	115.8 (6)	116.42 (17)	116.6 (3)
O3—N1—O1	119.5 (4)	119.72 (7)	121.03 (19)	121.6 (6)	121.58 (17)	121.8 (3)
O3—N1—O2	122.5 (4)	121.83 (7)	121.7 (2)	122.5 (6)	122.00 (18)	121.6 (3)
C2—C1—N0	119.0 (6)	119.35 (7)	118.5 (2)	119.0 (5)	120.02 (17)	119.7 (3)
C2—C1—C6	123.2 (5)	121.80 (8)	121.3 (2)	122.1 (5)	120.55 (18)	120.6 (3)
C6—C1—N0	117.8 (5)	118.85 (7)	120.2 (2)	118.9 (6)	119.42 (16)	119.7 (3)

Table 3.11: Hydrogen-bonding geometries (Å; º) for sugar/needle like compounds 1b, 2b, 3b-M and 3b-P

D*—H···*A	***D*···*A*; *D*—H···*A***			
	1b	**2b**	**3b-M**	**3b-P**
N0—H1*N*···O2^{i}	2.8792 (9); 175.7 (8)	2.944 (3); 165 (2)	2.931(2); 162.3(4)	2.853(3);170.7 (8)
N0—H1*N*···O1^{i}			3.040 (2); 139.8 (6)	3.221 (3); 120.2(9)
N0—H2*N*···O1^{ii}	2.8598 (9); 177.3 (8)	2.822 (3); 176 (2)	2.824 (4); 172.6 (6)	2.975 (3); 173.0 (7)
N0—H3*N*···O1^{iii}	2.8117 (9);171.4 (9)	2.797 (3);163 (2)	2.826 (2); 177.6 (6)	2.839 (4); 173.4 (3)

Table 3.12: Hydrogen-bonding geometries (Å; º) for sugar/needle like compounds 1a and 3a

D*—H···*A	***D*···*A*; *D*—H···*A***	
	1a	**3a**
N0—H1*N*···O2^{i}	2.878 (2); 172. 5 (3)	2.923(2);159.4 (9)
N0—H1*N*···O1^{i}		3.031(2);142.1 (5)
N0—H2*N*···O1^{ii}	2.860 (6); 175.8 (2)	2.841(3); 168.0 (8)
N0—H3*N*···O1^{iii}	2.813 (6);172.5 (5)	2.821(4); 175.4 (6)

CCDC No. 1009873, 1009874, 967489, 841664, 967496 and 967495 contains the crystallographic data for the compounds **1a**, **3a**, **3b-M**, **3b-P**, **4b** and **5b** respectively. This data can be obtained free of charge via http://www.ccdc.cam.ac.uk/conts/retrieving.html, or from the Cambridge Crystallographic Data Centre, 12 Union Road, Cambridge CB2 1EZ, UK; fax: (+44) 1223 336 033; or e-mail: deposit@ccdc.cam.ac.uk.

3.8 Variable temperature FT-IR

Deeper insight of the ferroelectric phase transition was further explored by spectroscopic techniques. Infrared spectroscopy experiments have provided detailed information on soft modes and lattice vibrational properties of ferroelectric crystals.

To check the reason for ferroelectricity in hair like crystal only and not in sugar/needle like crystals we performed variable temperature FT-IR on compounds **1a, 1b, 3a and 3b** (Figure 3.28 a-d) and compare with FT-IR spectra of ferroelectric KNO_3 phase [31].

In-plane bending mode (υ_4) of NO_3^- ion at 725 cm^{-1} disappeared with increase in temperature in compound **1a/1b**. Weak Band at 750 cm^{-1} gets merged into strong band at 742 cm^{-1} corresponding to *in-plane* ring deformation mode with temperature.

FT-IR spectra of **1a** contain two bands at 821 and 834 cm^{-1} while **1b** contain single band at 825 cm^{-1}. Splitting of this mode into a *doublet* may be due to lowering of symmetry of the NO_3^- ion from D_{3h} to C_{2v} or *Cs* which is essential requirement of ferroelectric material. Similar observations of two bands in **1a** and one band in **1b** are matches with ferroelectric phase and paraelectric phase of KNO_3 respectively.

FT-IR spectra confirm the para-electric nature of **1b** (Figure 3.28d) as it matches with para-electric phase of KNO_3-II at 295K (Figure 3.28e) while the **1a** showed ferroelectric nature at 295 K (Figure 3.28c) due to presence of two bands (υ_2 mode) as in KNO_3-III phase (406K). As the temperature increased the para electric nature of **1b** remains same while **1a** changes from ferroelectric to paraelectric phase with diminishing υ_2 band as observed in KNO3-I (419K). Similar observation was found in $NaNO_3$ in which extra band of υ_2 mode increased dramatically in intensity at the expense of υ_2 with increased temperature i.e. high temperature phase-II. In case of $NaNO_3$, additional peaks were interpreted as arising from non-critical structural fluctuations into domains of a monoclinic phase [32]. These results explain the ferroelectric character of nitrate salts. Hence observation of ferroelectricity in **1a** and not in **1b** is proved at room temperature.

The bands at 960-912 cm^{-1} corresponding to N-H---O hydrogen bonding almost get disappeared with increase in temperature. The variation of υ_1 band (symmetric stretching) revealed the phase transformation distinctively. The variations in the spectra measured

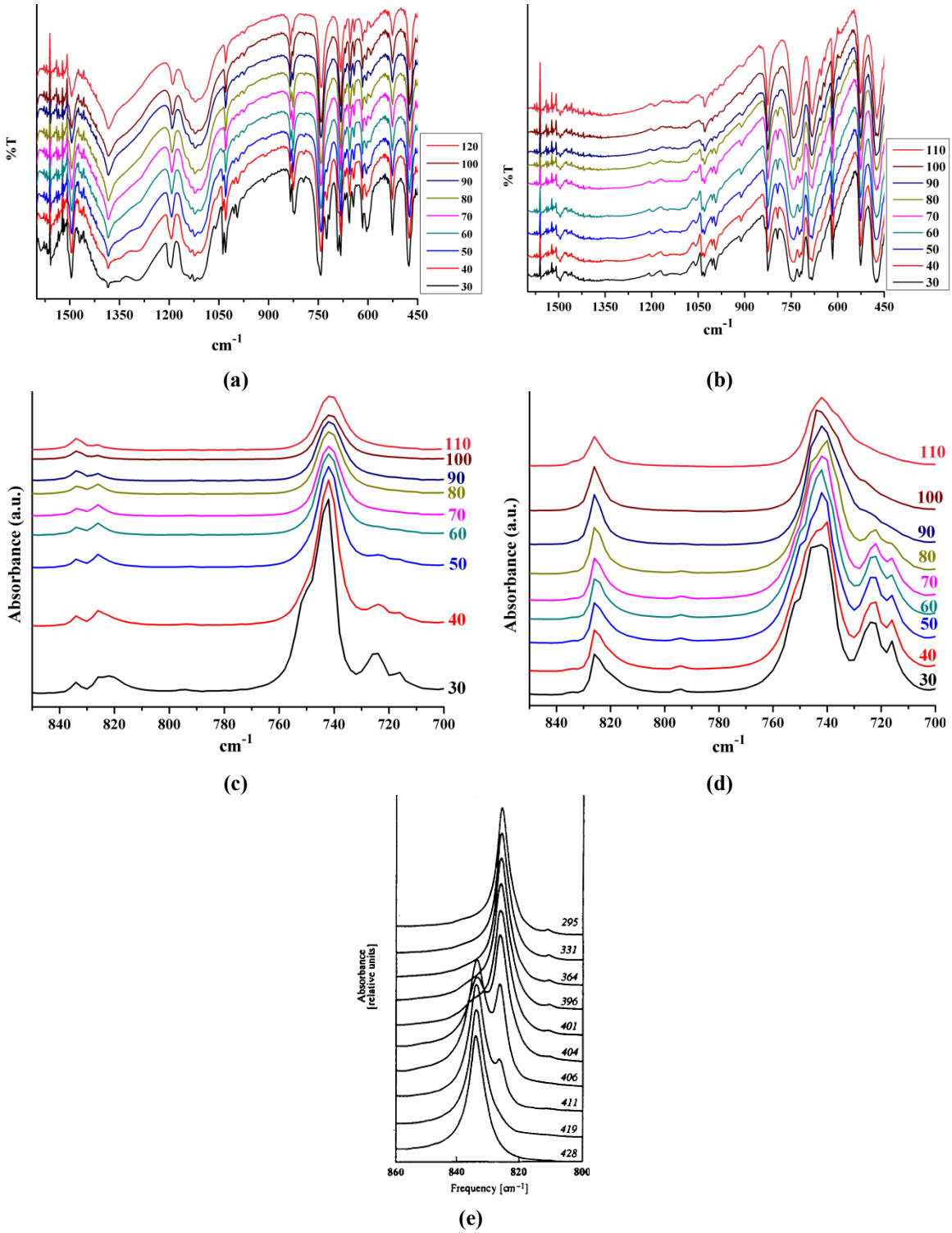

Fig. 3.28: (a & c) variable temperature FT-IR of 1a; (b & d) variable temperature FT-IR of 1b and (e) variable temperature FT-IR of KNO_3

from 30°C to 110°C clearly demonstrated the transformation from phase-I to phase-II as shown in Figure 3.28 a-b. It clearly shows disappearance of doublet at 1030 and 1037 cm^{-1} of phase-I of **1a** and appearance of one band at 1028 cm^{-1} of phase-II. Similar observation was found in compound **1b**.

The C-C and C-N stretching vibrations observed at 993 cm^{-1} also get reduced and shift by 6 cm^{-1} to 987 cm^{-1} with increase in temperature. C-N stretching at 1202 cm^{-1} and 1194 cm^{-1} gets merged into one another and single band at 1191 cm^{-1} appear.

The band at 1340-1350 cm^{-1} characteristic for the anti-symmetric stretching (υ_3) mode of nitrate anion, decreases steadily with increasing temperature of isothermal heating.

The N-H vibrations observed at 3140-2600 cm^{-1} also get reduced in intensity and shifted slightly in case of **1a/1b** while in **1a** doublet band (2637 and 2605 cm^{-1}) gets merged into single band (2591 cm^{-1}) suggesting the rearrangement of cation and hydrogen bonding at higher temperature.

All bands which show changes in the form of reduced intensity, splitting and disappearance show complete reversibility after cooling.

Comparing FT-IR spectra of **3a/3b** (Figure 3.29 c-d) with **1a/1b** in the region of 850-700cm^{-1} one can notice that the intensity of weak and strongest bands observed in the spectrum of anilinium nitrate (**1a/1b**) at 821-840 cm^{-1} and 725 cm^{-1} is in opposite relation to that observed at 825 cm^{-1} and 729 cm^{-1} in the FT-IR spectrum of compound **3a/3b**.

No change was observed in *in-plane* bending mode (υ_4) at 728cm^{-1} with change in temperature in **3a**/**3b**. FT-IR spectra of **3a and 3b** in which band at 825/826cm^{-1} itself splited into two bands at 821 cm^{-1} and 825 cm^{-1} corresponds to out-of-plane bending (υ_2) of NO_3^- ion. As the temperature increased bands in **3a** get merged into one another and formed a single band at 825 cm^{-1} while in case of **3b**, two bands get merged and formed single band at 821 cm^{-1}. This might be the reason behind ferroelectricity observed in **3a** and not in **3b**.

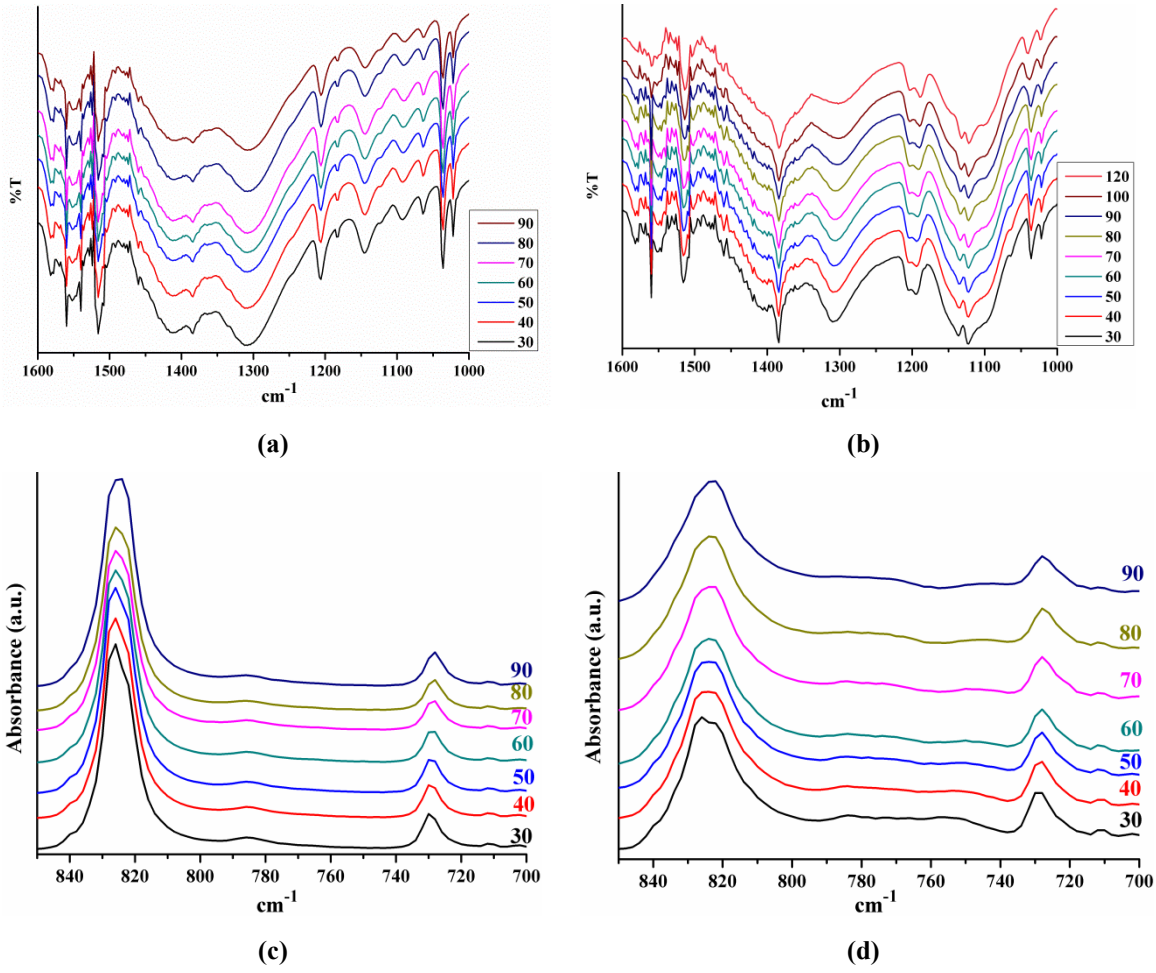

Fig. 3.29: (a & c) variable temperature FT-IR of 3a and (b &d) variable temperature FT-IR of 3b

The bands at 968cm^{-1} correspond to C-H out-of-plane deformation mode decreases with increase in temperature. No change was observed in υ_1 band (symmetric stretching) of **3a**/**3b** doublet at 1030 cm^{-1} and 1037 cm^{-1} of phase-I with temperature. C–N stretching band is stronger and well separated in intensity in **3a** while of exactly opposite character in **3b**.

It is seen that the intensity of two strong bands (1383 cm^{-1} and 1310 cm^{-1}) corresponding to N–H$^{\cdots}$O in-plane deformation modes in the spectrum of **3a** are having opposite relation observed in **3b**. No change is observed in N–H$^{\cdots}$O in-plane deformation modes with temperature. The N-H vibrations observed at 3112-2600 cm^{-1} also show reduction in intensity and slight shifting while doublet bands (2631 and 2644 cm^{-1}) gets merged into a single band at 2621 cm^{-1} in **3b** near phase transition temperature. No significant change was observed for compound **3a** in this region.

3.9 Conclusion

- We successfully designed, synthesized and characterized series of 4-alkyl substituted aniline nitrate salts using IR, ^{1}H NMR and Single crystal XRD.
- All compounds are investigated for structural phase transitions using TG/DTA, DSC, single crystal XRD and Variable Temperature IR.
- DSC measurements showed solid-solid reversible phase transition for all compounds except compound **4b**.
- Ferroelectric measurement showed hysteresis loop at room temperature for compounds **1a** ($P_S = 1.71 \mu Ccm^{-2}$) and **3a** ($P_S = 2.09 \mu Ccm^{-2}$).
- Single crystal study showed presence of helical chain in **2b** and **3a/3b** due to H-bonding.
- Compound **3b** crystallizes in two forms with distinctly different helical chains. The separated crystals have left handed (3b-M) and right handed (3b-P) chains.
- CD spectra confirm the enantiomeric nature of the optically active compounds i.e. compounds **3b-M** and **3b-P**.
- Symmetry lowering of the NO_3^- ion from D_{3h} to C_{2v} was found in the compound **1a** confirm by room temperature FT-IR.
- **3a/3b** was found to undergo solid–solid phase transitions: Ferroelastic ($P2_12_12_1$) I 295 K →paraelectric II (*Pbca*) second-order type.
- The single crystal x-ray and calorimetric studies suggest an 'order–disorder' mechanism for the ferroelectric phase transition.
- The ferroelectric phase transition (II →I) mechanism is due to the dynamics of 4-ethyl anilinium cations contributing predominantly to the spontaneous polarization.

- Loss of domains during phase transition in **3b** confirms Ferroelastic character confirmed by polarizing microscope.

- Variable Temperature dependent IR and SXRD study confirmed the change in modes of NO_3^- ion as well ring at phase transition temperature confirming the changes in structure is of order-disorder structure.

- The crystal structure of **3b** at HT, phase II, has highly disordered cations distributed over two sites (occupancy 0.50/0.50). At low temperature (RT), in phase I all the cations are fully ordered.

- By destructing the regular planar arrangement between nitrate anion and ammonium cation to allow latter to act as a stator we designed room temperature ferroelectricity in a KNO_3 type molecular compounds, a true '**Molecular Ferroelectric**'.

3.10 References

[1] (a) K. M. Ok, E. O. Chi, P. S. Halasyamani, *Chem. Soc. Rev.* **2006**, *35*, 710-717; (b) G. H. Haertling, *J. Am. Ceram. Soc.* **1999**, *82*, 797-818; (c) J. F. Scott, *Ferroelectric memories, Vol. 3*, Springer, **2000**; (d) R. Ramesh, N. A. Spaldin, *Nat. Mater.* **2007**, *6*, 21-29; (e) N. A. Spaldin, M. Fiebig, *Science* **2005**, *309*, 391-392.

[2] D. A. Bonnell, *Science* **2013**, *339*, 401-402.

[3] (a) A. S. Tayi, A. K. Shveyd, A. C. H. Sue, J. M. Szarko, B. S. Rolczynski, D. Cao, T. J. Kennedy, A. A. Sarjeant, C. L. Stern, W. F. Paxton, W. Wu, S. K. Dey, A. C. Fahrenbach, J. R. Guest, H. Mohseni, L. X. Chen, K. L. Wang, J. F. Stoddart, S. I. Stupp, *Nature* **2012**, *488*, 485-489; (b) M. E. Lines, A. M. Glass, *Principles and applications of ferroelectrics and related materials*, Clarendon press Oxford, **2001**.

[4] (a) L. Cross, R. Newnham, *J. Am. Ceram. Soc.* **1987**, *11*, 289-305; (b) W. Martienssen, H. Warlimont, Springer Handbook of Condensed Matter and Materials Data, **2005**; (c) Y. Shiozaki, E. Nakamura, T. Mitsui, *Ferroelectrics and Related Substances*, Springer, **2006**; (d) K. Müller, Y. Luspin, J. Servoin, F. Gervais, *J. Phys. Lett.-Paris* **1982**, *43*, 537-542; (e) G. K. Aggarwal, A. Kumar, U. Naithani, *International Journal of Modern Engineering Research (IJMER) Vol* **2012**, *2*.

[5] J. Valasek, *Phys. Rev.* **1921**, *17*, 475.

[6] J. Li, Y. Liu, Y. Zhang, H.-L. Cai, R.-G. Xiong, *Phys. Chem. Chem. Phys.* **2013**, *15*, 20786-20796.

[7] (a) U. Caruso, R. Centore, B. Panunzi, A. Roviello, A. Tuzi, *E. J. Inorg. Chem.* **2005**, *2005*, 2747-2753; (b) R. Centore, A. Tuzi, *Acta Crystallogr. Sect. C* **2001**, *57*, 698-701; (c) R. Centore, A. Roviello, A. Tuzi, B. Panunzi, *Acta Crystallogr. Sect. C* **2002**, *58*, 26-28.

[8] R. Centore, M. Jazbinsek, A. Tuzi, A. Roviello, A. Capobianco, A. Peluso, *Cryst. Eng. Comm.* **2012**, *14*, 2645-2653.

[9] A. D. Mighell, V. L. Himes, J. R. Rodgers, *Acta Crystallogr. Sect. A* **1983**, *39*, 737-740.

[10] A. I. Kitaigorodskii, in Organic Chemical Crystallography, Consultant Bureau, New York, NY, 1961.

[11] C. N. R. Rao, B. Prakash, M. Natarajan, *Nat. Stand. Ref. Data Ser. Nat. Bur. Stand.* **1975**, 1-48

[12] (a) H. Lu, J. Hardy, *Phys. Rev. B* **1991**, *44*, 7215; (b) M. J. Harris, *Solid State Commun.* **1992**, *84*, 557-561.

[13] (a) N. Kumar, R. Nath, *IEEE Trans. Dielectr. Electr. Insul.* **2005**, *12*, 1145-1150; (b) N. Kumar, R. Nath, *J. Appl. Phys.* **2005**, *97*, 24105-24106; (c) N. Dabra, J. S. Hundal, K. C. Sekhar, A. Nautiyal, R. Nath, *J. Am. Ceram. Soc.* **2009**, *92*, 834-838; (d) N. Dabra, J. S. Hundal, K. C. Sekhar, A. Nautiyal, R. Nath, *IEEE Trans. Ultrason., Ferroelectr., Freq. Control* **2009**, *56*, 1627-1633.

[14] (a) A. Sieradzki, J. Komar, E. Rysiakiewicz-Pasek, A. Ciżman, R. Poprawski, *Ferroelectrics* **2010**, *402*, 60-65; (b) S. V. Baryshnikov, E. V. Charnaya, A. Y. Milinskiy, E. V. Stukova, C. Tien, D. Michel, *J. Phys.: Condens. Matter.* **2009**, *21*, 325902; (c) D. Yadlovker, S. Berger, *Appl. Phys. Lett.* **2007**, *91*, - 173104

[15] (a) E. Ramachandran, S. Natarajan, *Cryst. Res. Technol.* **2004**, *39*, 308-312; (b)H. Kusumoto, T. Kaito, S.-i. Yanagiya, A. Mori, T. Inoue, *J. Cryst. Growth* **2005**, *277*, 536-540; (c) H. K. Henisch, *Crystal growth in gels*, Courier Dover Publications, **1996**.

[16] (a) A. R. Patel, A. V. Rao, *Bull. Mater. Sci.* **1982**, *4*, 527-548; (b) N. Miyazaki, Y. Matsuura, D. Imahase, *J. Cryst. Growth* **2006**, *289*, 659-662.

[17] M. Marchewka, A. Pietraszko, *J. Phys. Chem. Solids* **2005**, *66*, 1039-1048.

[18] M. K. Marchewka, J. Janczak, S. Debrus, J. Baran, H. Ratajczak, *Solid State Sci.* **2003**, *5*, 643-652.

[19] (a) R. Murugan, A. Ghule, H. Chang, *J. Appl. Phys.* **1999**, *86*, 6779-6788; (b) R. Murugan, P. J. Huang, A. Ghule, H. Chang, *Thermochim. Acta* **2000**, *346*, 83-90; (c) M. Balkanski, M. Teng, M. Nusimovici, *Phys. Rev.* **1968**, *176*, 1098.

[20] M. Magdalena Szostak, H. Chojnacki, *Opt. Mater.* **2011**, *33*, 1395-1397.

[21] E. J. Freney, L. A. Garvie, T. L. Groy, P. R. Buseck, *Acta Crystallogr., Sect. B: Struct. Sci.* **2009**, *65*, 659-663.

[22] F. El-Kabbany, S. Taha, E. El-Khawas, *J. Mater. Sci.* **1989**, *24*, 1819-1826.

[23] (a) S. Sawada, S. Nomura, S. i. Fujii, *J. Phys. Soc. Jpn.* **1958**, *13*, 1549-1549; (b) S. Sawada, S. Nomura, Y. Asao, *J. Phys. Soc. Jpn.* **1961**, *16*, 2486-2494.

[24] (a) M. Marchewka, A. Pietraszko, *J. Phys. Chem. Solids* **2005**, *66*, 1039-1048; (b) P. S. Ghalsasi, A. K. Vishwakarma, *Cryst. Eng. Comm* **2010**, *12*, 1693-1695.

[25] R.-j. Xu, *Acta Crystallogr. Sect. E: Struct. Rep. Online* **2010**, *66*, o835-o835.

[26] L. Bourgeois, B. Toudic, C. Ecolivet, P. Bourges, T. Breczewski, *TC*, *20*, 21.23.

[27] M. Tello, A. Lopez-Echarri, J. Zubillaga, I. Ruiz-Larrea, F. Zuniga, G. Madariaga, A. Gomez-Cuevas, *J. Phys.: Condens. Matter* **1994**, *6*, 6751.

[28] H. Wondratschek, U. Müller, *International Tables for Crystallography*, International Union of Crystallography, **2004**.

[29] J. Sapriel, *Phys. Rev. B* **1975**, *12*, 5128.

[30] A. R. Lim, D. K. Park, J.-H. Chang, S.-Y. Jeong, *J. Phys. Soc. Jpn.* **2001**, *70*, 1937-1941.

[31] (a) R. Khanna, J. Lingscheid, J. Decius, *Spectrochim. Acta* **1964**, *20*, 1109-1116; (b) M. A. Ismail, U. A. Jayasooriya, S. F. Kettle, *J. Chem. Phys* **1983**, *79*, 4459-4462; (c) A. Shultin, S. Karpov, *J. Phys. Chem. Solids* **1969**, *30*, 1981-1988.

[32] M. J. Harris, E. K. H. Salje, B. K. Guttler, *J. Phys.: Condens. Matter* **1990**, *2*, 5517.